J. Fluid Mech. (2020), *vol*. 902, A17.
Published by Cambridge University Press
doi:10.1017/jfm.2020.436

Acoustic feedback loops for screech tones of underexpanded free round jets at different modes

Xiang-Ru Li[1], **Xi-Wen Zhang**[1], **Peng-Fei Hao**[1] **and Feng He**[1],†

[1]Department of Engineering Mechanics, School of Aerospace, Tsinghua University, Beijing 100084, PR China

(Received 31 October 2019; revised 9 May 2020; accepted 23 May 2020)

The flow structures and the acoustic feedback loops of underexpanded round jets are investigated by numerical simulations. The jets have a Mach number of 1 at the nozzle exit and a diameter-based Reynolds number of 2.5×10^3. Three nozzle pressure ratios (NPRs) of 2.2, 2.4 and 2.6 are considered. The wavelengths of the screech tones are in good agreement with the experimental measurements on high-Reynolds-number jets in the literature. The screech tones are respectively at the A1 and B modes for the jets at NPRs of 2.2 and 2.6. Two screech tones at the A2 and B modes are identified in the jet at the NPR of 2.4 and the wavelet analyses conducted on the pressure fluctuations confirm that these two modes are contemporaneous. The amplitude and phase fields of fluctuating pressure at the screech frequencies are presented in the nozzle exit plane and azimuthal planes. The effective source locations of the screech tones are determined based on the distributions of the phase. The number of periods contained in the screech feedback loop is equal to the number of cells in the standing wave between the nozzle exit and the effective source. The screech frequencies estimated by the classical feedback model agree well with the numerical results at different modes. A modified model, in which the classical feedback model and the upstream-propagating acoustic wave mode of the jet are combined, shows that the screech feedback loops at the A1 and A2 modes are associated with the same acoustic wave mode. The modified model fails to estimate the screech frequencies at the B mode. Different feedback mechanisms lead to the coexistence of the A2 and B modes. The coherent structures corresponding to different screech modes are extracted by dynamic mode decomposition.

Key words: jets, jet noise, aeroacoustics

1. Introduction

A supersonic jet operating at imperfectly expanded conditions is characterized by quasi-periodic shock structures in the jet plume. In this case, the noise of the jet comprises three basic components: the turbulent mixing noise, the broadband shock-associated noise and the screech tone (Tam 1995). The screech tone first observed by Powell (1953) has a high-amplitude discrete frequency. The development of the understanding of the screech tone is summarized in some detailed reviews, such as Raman (1999) and Edgington-Mitchell (2019). Based on the schlieren flow visualization, Powell (1953)

† Email address for correspondence: hefeng@tsinghua.edu.cn

suggested that the generation of the screech tone is due to an acoustic feedback cycle near the nozzle exit. The detailed structures of the screech feedback loop are described in Tam (1995).

For an axisymmetric underexpanded jet, the frequency of the screech tone decreases continuously with the increase of the nozzle pressure ratio (NPR). However, at some particular conditions, the screech frequency jumps, which means the change of the screech mode. Powell (1953) identified four screech modes for round jets, and named these modes A, B, C and D. The switches between these modes are usually accompanied with the changes of the azimuthal characteristics of the sound fields and flow structures. Furthermore, the experimental studies of Merle (1956), Davies & Oldfield (1962), Powell, Umeda & Ishii (1992) and Ponton & Seiner (1995) showed that the A1 and A2 modes are toroidal modes, the C mode corresponds to a helical mode, and the B and D modes are flapping or sinuous modes.

The unsteady motions of shocks are observed simultaneously with the generation of the screech tone. Panda (1998) demonstrated that the features of the shock oscillations are the same as the screech modes. At an axisymmetric mode, there are more motions in the core of the jet and the 'shock splitting' phenomenon is noted. Both the upstream-propagating acoustic disturbances and the downstream-propagating instability waves can influence the shock motions. In the cases of non-axisymmetric screech modes, the manners of the shock oscillations are more complex. In the helical C mode, the upper and lower half of the third shock cone appear and disappear in turn (Panda 1998). The shock oscillations at the antisymmetric B mode were discussed by Andre, Castelain & Bailly (2011) based on the schlieren photography. The shock motion is also in an antisymmetric pattern and the magnitude of the shock oscillation is clearly related to the screech amplitude.

The issues of the generation and the effective source location of the screech tone are crucial to understand the screech mechanism. The interaction between vortices and a shock was solved by the direct numerical simulation (DNS) in Suzuki & Lele (2003). They observed that the shock wave tends to leak near a saddle point between the vortices in the shear layer, and the shock-leakage process explains the generation of the screech tone. Berland, Bogey & Bailly (2007) performed a large-eddy simulation (LES) on an underexpanded planar jet. The flow visualizations of the third shock cell showed that the shock-leakage process occurs and produces the upstream-propagating sound waves. Panda (1999) investigated the generation process of the screech tone based on the phase-matched combined views of the schlieren photographs and pressure fluctuations. The time evolution of the near-field pressure fluctuations showed that the screech waves appear between the third and the fourth shock cell at the A2 mode. The generation mechanism of the screech tone at the C mode was studied by Umeda & Ishii (2001) through a series of instantaneous schlieren photographs. They found the dominant source is just downstream of the rear edge of the third shock cell. Gao & Li (2010) analysed the screech feedback loop based on their numerical simulation database (Li & Gao 2005, 2008). They found that the dominant sound sources are between the second and the fourth shock cell for the A1, A2, B and C modes. Edgington-Mitchell *et al*. (2014) conducted particle image velocimetry (PIV) measurements on an axisymmetric underexpanded jet at the C mode and suggested that the dominant acoustic source for the screech tone is between the second and the fourth shock. Based on the near-field acoustic measurements and the time-resolved schlieren visualizations, Mercier, Castelain & Bailly (2017) studied the acoustic feedback loops of the jets at different modes. They suggested that the single source of the screech tone is at the fourth shock tip for the A1 and A2 modes, and at either the third or the fourth shock tip for the B mode.

In some situations, multiple screech tones are presented in the noise spectra of rectangular and axisymmetric underexpanded jets (Raman 1999). The interactions between these tones and the issue on whether these tones are switching mutually or coexisting steadily need to be researched. Raman (1997) used the 'instantaneous spectra' to study the mode switches of the rectangular jets. The 'instantaneous spectra' were obtained by performing short-time fast Fourier transforms on smaller segments of a long data sequence. In different cases, the screech modes are either contemporaneous or in a mutually exclusive fashion. Walker, Gordeyev & Thomas (1997) experimentally studied the multiple acoustic modes and shear layer instability waves in an underexpanded jet via the Morlet wavelet transform. The wavelet analysis provided a very useful tool for understanding the intermittent or modulated behaviours in unsteady flows. The results showed that the multiple screech tones coexist at an operating condition.

Some numerical results (Shen & Tam 2002; Li & Gao 2008) also indicated that there are several screech tones at a given jet Mach number. Shen & Tam (2002) suggested that the two tones are coexisting whenever two screech tones are measured in the noise spectrum and the feedback acoustic disturbances can complete the screech feedback loop in two ways. The feedback process is closed by the upstream-propagating free-stream acoustic waves for the A1 and B modes and by the upstream-propagating neutral acoustic wave modes of the jets for the A2 and C modes. Different feedback mechanisms explain the coexistence of the screech tones. Recently, Gojon, Bogey & Mihaescu (2018) found that, for the C mode, there are upstream-propagating acoustic waves in the underexpanded jet that belong to the neutral acoustic modes of the equivalent ideally expanded jet. However, in contrast to the conclusions of Shen & Tam (2002), Edgington-Mitchell *et al*. (2018) demonstrated that the upstream-travelling wave that closes the A1 and A2 modes of the jet screech is the same upstream-propagating neutral acoustic mode. Mancinelli *et al*. (2019) experimentally observed that the A1 and A2 modes are mutually exclusive during the mode staging process.

The main purposes of this paper are to investigate the characteristics of the screech feedback loops at different modes and to explore the mode staging process between the A2 and B modes. In the present study, numerical simulations are conducted on three underexpanded round jets at different NPRs. These jets originate from a converging nozzle and have a Reynolds number of 2.5×10^3. The results of numerical solutions are compared with experimental data for validation. Detailed analyses on the screech feedback loops are conducted based on the numerical results. The paper is organized as follows. The governing equations and numerical methods for the present simulations and a mesh independence study are shown in § 2. The results of the numerical simulations such as the screech frequencies, effective source locations and the convection velocities of the instability waves in the shear layer are presented in § 3. In § 4, two acoustic feedback models with different upstream-propagating components are analysed to study the coexistence mechanism of the A2 and B modes. In § 5, the coherent structures related to different screech modes are discussed by dynamic mode decomposition (DMD) analyses. Concluding remarks are given in § 6.

2. Simulation details

2.1. *Governing equations and numerical methods*

The unsteady compressible Navier–Stokes equations for a perfect gas in a cylindrical coordinate system are considered in the present simulations. The ambient physical parameters, including the density ρ_∞, sound velocity a_∞, temperature T_∞, molecular

viscosity μ_∞ and the nozzle exit diameter D are used to non-dimensionalize the equations. The non-dimensional equations are as follows:

$$\frac{\partial U}{\partial t} + \frac{\partial A}{\partial x} + \frac{\partial B}{r\partial \theta} + \frac{\partial C}{\partial r} + \frac{1}{r}D = 0, \tag{2.1}$$

$$U = \begin{pmatrix} \rho \\ \rho u_x \\ \rho u_\theta \\ \rho u_r \\ \rho E \end{pmatrix}, \tag{2.2}$$

$$A = \begin{pmatrix} \rho u_x \\ \rho u_x u_x + p - \tau_{xx} \\ \rho u_\theta u_x - \tau_{\theta x} \\ \rho u_r u_x - \tau_{rx} \\ \rho H u_x + q_x - u_x \tau_{xx} - u_\theta \tau_{\theta x} - u_r \tau_{rx} \end{pmatrix},$$

$$B = \begin{pmatrix} \rho u_\theta \\ \rho u_x u_\theta - \tau_{x\theta} \\ \rho u_\theta u_\theta + p - \tau_{\theta\theta} \\ \rho u_r u_\theta - \tau_{r\theta} \\ \rho H u_\theta + q_\theta - u_x \tau_{x\theta} - u_\theta \tau_{\theta\theta} - u_r \tau_{r\theta} \end{pmatrix},$$

$$C = \begin{pmatrix} \rho u_r \\ \rho u_x u_r - \tau_{xr} \\ \rho u_\theta u_r - \tau_{\theta r} \\ \rho u_r u_r + p - \tau_{rr} \\ \rho H u_r + q_r - u_x \tau_{xr} - u_\theta \tau_{\theta r} - u_r \tau_{rr} \end{pmatrix},$$

$$D = \begin{pmatrix} \rho u_r \\ \rho u_x u_r - \tau_{xr} \\ 2\rho u_\theta u_r - 2\tau_{\theta r} \\ \rho u_r u_r - \tau_{rr} - \rho u_\theta u_\theta + \tau_{\theta\theta} \\ \rho H u_r + q_r - u_x \tau_{xr} - u_\theta \tau_{\theta r} - u_r \tau_{rr} \end{pmatrix}.$$

Here x, θ, r denote the axial, azimuthal and radial directions; u_x, u_θ, u_r are the non-dimensional velocities in the x, θ, r directions, respectively; and ρ and p are non-dimensional density and pressure. The non-dimensionalization results in the dimensionless parameter $Re = \rho_\infty c_\infty D/\mu_\infty$. The total energy is defined as $E = T/[\gamma(\gamma - 1)] + 1/2 u_i u_i$, with the specific heat capacity ratio $\gamma = 1.4$. The non-dimensional temperature T is obtained through the non-dimensional equation of state for an ideal gas:

$$p = \frac{\rho T}{\gamma}. \tag{2.3}$$

The viscous stress term τ_{ij} is given by the Newtonian linear stress–strain relation

$$\tau_{ij} = \frac{\mu}{Re}\left(2S_{ij} - \frac{2}{3}\delta_{ij}S_{kk}\right), \tag{2.4}$$

and the heat-flux-vector components are

$$\left.\begin{aligned} q_x &= \frac{-\mu}{Pr(\gamma-1)Re}\frac{\partial T}{\partial x}, \\ q_\theta &= \frac{-\mu}{Pr(\gamma-1)Re}\frac{\partial T}{r\partial \theta}, \\ q_r &= \frac{-\mu}{Pr(\gamma-1)Re}\frac{\partial T}{\partial r}, \end{aligned}\right\} \tag{2.5}$$

where the Prandtl number is taken as $Pr = 0.72$ and the molecular viscosity is computed by Sutherland's law (Schlichting & Gersten 2016).

At underexpanded conditions, periodic shock cells appear in the jet flow. To capture the discontinuities caused by the shocks, the flux-vector splitting (Steger & Warming 1981) and a seventh-order weighted essentially non-oscillatory (WENO) scheme are employed on the inviscid fluxes. The original finite-difference WENO scheme introduced by Balsara & Shu (2000) is optimized by means of limiters (Wu & Martin 2007) to reduce the numerical dissipation. A relative limiter on the total variation is employed during the simulation. The specific form of the limiter and the associated threshold values are given by equation (17) in Wu & Martin (2007). The viscous fluxes are discretized by using a standard sixth-order central difference scheme. The temporal integration is performed by the four-stage third-order strong stability-preserving Runge–Kutta technique (Ruuth & Spiteri 2004).

2.2. *Jet parameters and simulation set-up*

Three numerical simulations of underexpanded round jets with different NPRs are conducted. The NPR is defined as the ratio between the stagnation pressure p_0 upstream of the nozzle and the ambient pressure p_∞. The ambient temperature T_∞ and density ρ_∞ are 288 K and 1.225 kg m^{-3}. The stagnation temperature T_0 for the cold jets considered here is equal to the ambient temperature. Three NPRs of 2.2, 2.4 and 2.6 are considered. These three jets have an identical Reynolds number of $Re = 2.5 \times 10^3$. The nozzle possesses an exit diameter of D and the width of the nozzle lip is $D/3$. The jet originates from the converging circular nozzle with an exit Mach number $M_e = 1$. At the nozzle exit, the centreline flow variables are given by the ideal gas isentropic relations. The pressure is uniform at the exit. A polynomial approximation of the Blasius profile (Bogey & Bailly 2010) with the boundary layer thickness $\delta = 0.05D$ is imposed for the axial velocity. The temperature is determined by the Crocco–Busemann relation (Schlichting & Gersten 2016). The radial and azimuthal velocities are set to zero.

The computational domain is taken from $-2D$ to $35D$ in the x direction and from 0 to $10D$ in the r direction. The nozzle exit is located at $x = 0$. At the outflow and lateral boundaries of the computational domain, the time-dependent non-reflecting boundary conditions (Thompson 1987, 1990) are implemented. The single-valued reconstruction (Morinishi, Vasilyev & Ogi 2004) is employed to satisfy the single-valued property at the axis. The no-slip adiabatic boundary condition is applied on the nozzle walls. Initially, the flow of the entire computational domain is set as the quiescent flow conditions. In each numerical case, a total of 250 000 iterations are computed after the transient period. The non-dimensional time step is set as 2×10^{-4}, permitting a non-dimensional simulation time of 50. A total of 1000 instantaneous full three-dimensional flow fields are stored with a time interval of 0.05. The resolvable non-dimensional frequency is up to 10.

Case	$n_x \times n_\theta \times n_r$	Number of grids	n_r^{radius}	n_r^{δ}	$\Delta r(r = 0.5)$	$\Delta x(x = 0)$
MESH1	$720 \times 64 \times 240$	11 million	60	7	$D/177$	$D/50$
MESH2	$720 \times 96 \times 240$	16.6 million	60	7	$D/177$	$D/50$
MESH3	$864 \times 96 \times 280$	23.2 million	70	9	$D/200$	$D/70$

TABLE 1. Grid characteristics of the numerical simulations at NPR = 2.2. Numbers of grid points (n_x, n_θ, n_r) in $(x,\ \theta,\ r)$ directions, the total number of grid points, the number of points within the nozzle radius n_r^{radius}, the number of points within the boundary layer at the nozzle exit n_r^{δ} and the mesh spacings Δr and Δx at the nozzle lip.

2.3. *Mesh independence*

In this section, the dependence of the numerical results on the grid resolution is investigated by a series of numerical simulations performed on the jet at the NPR of 2.2. The grid points are clustered near the nozzle exit and the shear layer by algebraic transformations. Table 1 gives the grid characteristics at different resolution levels. All of these cases are identical except for the mesh parameters listed in table 1. The case MESH2 has the same axial and radial grid resolutions as the case MESH1 but more grid points in the azimuthal direction. The case MESH3 has the same azimuthal grid points as the case MESH2 but higher grid resolutions in the axial and radial directions. Thus, the effects of the grid resolutions in different directions can be investigated by comparing the results of these three cases.

Figure 1(*a*) shows the distributions of the mean axial velocity on the centreline for these three cases. All of these curves show a good agreement, indicating that the mean velocity and the sizes of the shock cells are insensitive to the grid resolution. The noise spectra in the nozzle exit plane are represented in figure 1(*b*). The fundamental screech tone is evident at $St_j = 0.5804$ and a smaller peak associated with the second harmonic is visible at $St_j = 1.18$. The Strouhal number is defined as $St_j = fD_j/U_j$, where f is the non-dimensional frequency, U_j is the non-dimensional ideally expanded velocity and D_j is the non-dimensional ideally expanded equivalent jet diameter. Good agreement is achieved at the frequencies and amplitudes of the screech tone and the second harmonic. These comparisons indicate that the grid in the case MESH3 has sufficient resolution. Thus, this grid is used for the simulations at the NPRs of 2.4 and 2.6. In the following sections, more evidence is displayed to demonstrate the numerical accuracy of the present simulations.

3. Numerical results

3.1. *Flow snapshots*

The vortical structures in the shear layer and the acoustic fields of the jets at NPRs of 2.2, 2.4 and 2.6 are provided in figure 2 and in supplementary movies (available at https://doi.org/10.1017/jfm.2020.436). For the convenience of display, a coordinate transformation has been performed from cylindrical coordinates to Cartesian coordinates by

$$X/D = x, \quad Y/D = r\cos\theta, \quad Z/D = r\sin\theta. \tag{3.1a,b,c}$$

The jets originate from the nozzle with laminar conditions. As shown in figure 2(*a*) and supplementary movie 1, several axisymmetric vortex rings appear in the shear layer of the jet at the NPR of 2.2. The vortex rings gradually lose their symmetry characteristic

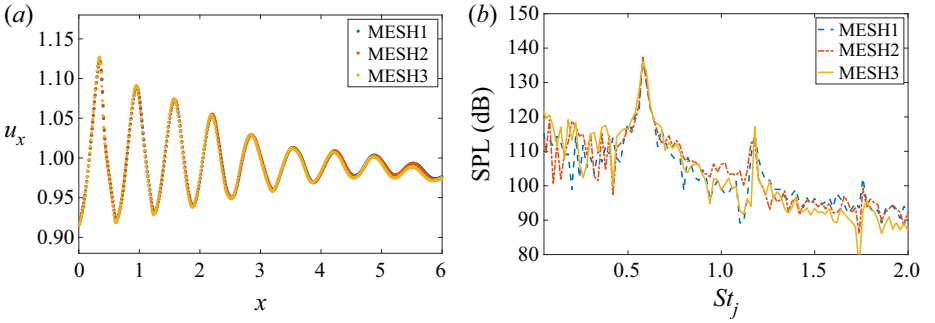

FIGURE 1. Comparisons of (*a*) the mean axial velocity distributions along the jet centreline and (*b*) the noise spectra at $(x, \theta, r) = (0, \pi/2, 2)$ of numerical solutions with varying grid resolutions.

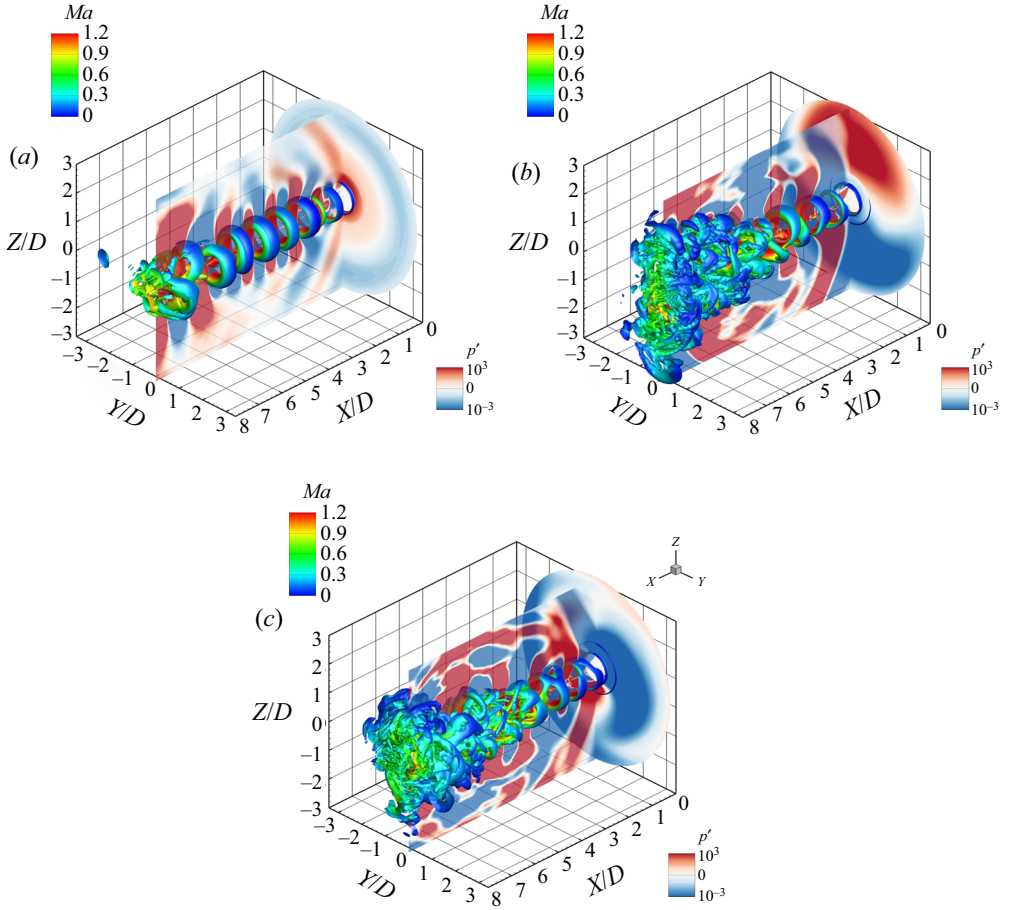

FIGURE 2. The instantaneous snapshots of the isosurfaces of the non-dimensional Q-criterion = 0.1, coloured by the local Mach number, and the pressure fluctuations in the planes $x = 0$, $\theta = \pi/2$ and $3\pi/2$ for the jets at (*a*) NPR = 2.2, (*b*) NPR = 2.4 and (*c*) NPR = 2.6. The nozzle exit is located at $X/D = 0$.

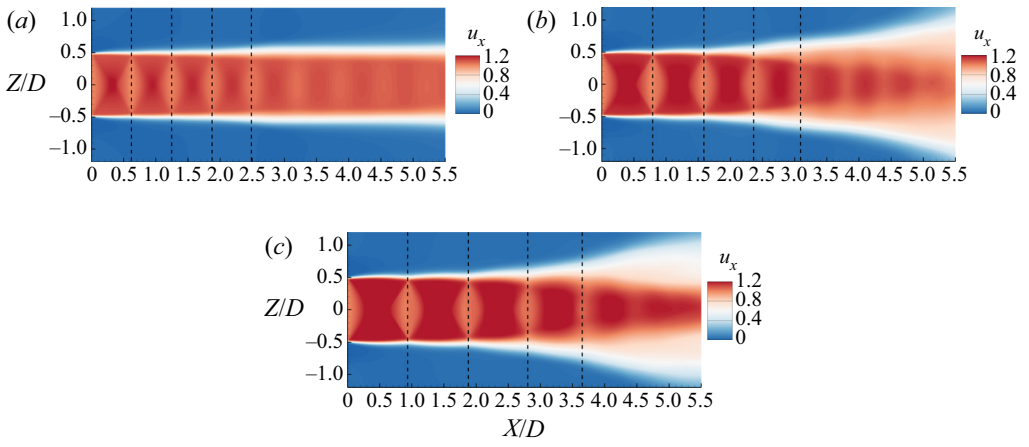

FIGURE 3. Axial mean velocity fields for the jets at (*a*) NPR = 2.2, (*b*) NPR = 2.4 and (*c*) NPR = 2.6. The black dashed lines indicate the axial positions of the shock reflection points at the jet shear layer.

when they move downstream. The acoustic waves propagating upstream or downstream are displayed by the fluctuating pressure fields in the planes $\theta = \pi/2$ and $3\pi/2$. The acoustic waves of the screech tone mainly propagate upstream and are symmetrical with respect to the jet axis. In the plane $X/D = 0$, the screech waves are shown as circles corresponding to the axisymmetric vortex rings in the shear layer.

Significant differences of vortical structures can be observed between the jets at NPRs of 2.2 and 2.4. As shown in figure 2(*b*) and supplementary movie 2, for the jet at the NPR of 2.4, the vortices are stronger around $\theta = \pi/2$ and $3\pi/2$. More complex vortices appear at downstream locations ($X/D \geq 5$) and the jet seems to transit into turbulence earlier than the jet at the NPR of 2.2. In the planes $\theta = \pi/2$ and $3\pi/2$, the upstream-propagating acoustic waves at the upper and lower sides of the jet have opposite phases. For the jet at the NPR of 2.6, vortices are also generated alternately on both sides of the jet, as shown in figure 2(*c*) and supplementary movie 3. The vortices in the shear layer as well as the acoustics field in the plane $X/D = 0$ have a more significant helical characteristic. For these three jets, the characteristics of the vortex structures and the screech waves are closely related. The modes of the screech tones will be discussed further in the following sections.

3.2. *Mean fields and shock cell spacing*

The spacing of the shock cell is an important length scale in locating the effective source of the screech tone. Mercier *et al.* (2017) found the effective sound source is at the third or fourth shock tip over a wide range of operating conditions. The axial mean velocity fields for different jets are shown in figure 3 and the first four shock reflection points at the shear layer are marked to obtain the shock cell spacings. The axial sizes of the shock cells increase with increasing NPR. An approximate solution for the spacing of the first shock cell was given by Pack (1950) based on a theoretical analysis:

$$\lambda_1 = 2.695\sqrt{(\mathrm{NPR}^{0.291} - 1.205)}. \tag{3.2}$$

NPR	λ_1 (numerical simulation)	λ_1 (equation (3.2))
2.2	0.62	0.6198
2.4	0.79	0.7864
2.6	0.93	0.9161

TABLE 2. Comparison of non-dimensional spacings of the first shock cell obtained from the numerical simulations and from equation (3.2).

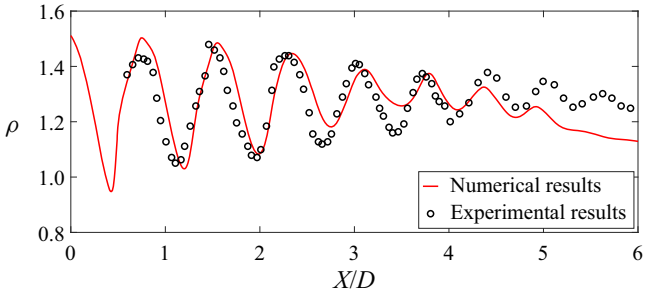

FIGURE 4. Comparison of non-dimensional averaged density along the jet centreline obtained from the numerical simulation and the experiment of Panda & Seasholtz (1999) at the NPR of 2.4.

Here the spacing of the first shock cell λ_1 is non-dimensionalized by the nozzle exit diameter D. In table 2, the spacing of the first shock cell obtained from the present numerical simulations and (3.2) are compared. Good agreement is found between the numerical and theoretical results. Moreover, the distribution of the averaged density along the centreline of the jet at the NPR of 2.4 is compared with the experimental results of Panda & Seasholtz (1999) in figure 4. The numerical results and the experimental results also show a good agreement. These results indicate that accurate spacings of shock cells can be obtained from the present simulations.

3.3. *Pressure spectra and tone frequencies*

Fast Fourier transforms are applied on the pressure fluctuations at every point along the circular line of $(x, r) = (0, 2)$ to obtain the frequencies and the azimuthal characteristics of the screech tones. As shown in figure 5(a), the amplitude of the screech tone at $St_j = 0.5804$ (the magenta arrow) distributes uniformly along the circular line $(x, r) = (0, 2)$. In figure 5(b), at different azimuthal angles, the phases of the screech tone are almost the same. These results indicate that the screech tone is at an axisymmetric mode for the jet at the NPR of 2.2. In figure 5(c), at the NPR of 2.4, the screech tone at $St_j = 0.4237$ (the magenta arrow) has higher amplitudes around the azimuthal angles of $\theta = \pi/2$ and $3\pi/2$, and becomes weak near $\theta = 0$ and π. As shown in figure 5(d), the phase of this screech tone abruptly changes around $\theta = 0$ and π resulting in a phase difference of π. Thus, this screech tone is at a flapping mode. In figure 5(c), there is another tone at $St_j = 0.5778$ (the blue arrow) which has almost equivalent amplitudes from $\theta = 0$ to 2π. As shown in figure 5(d), the phase of this tone continuously fluctuates along the circular line and the phase differences between different azimuthal angles are obviously

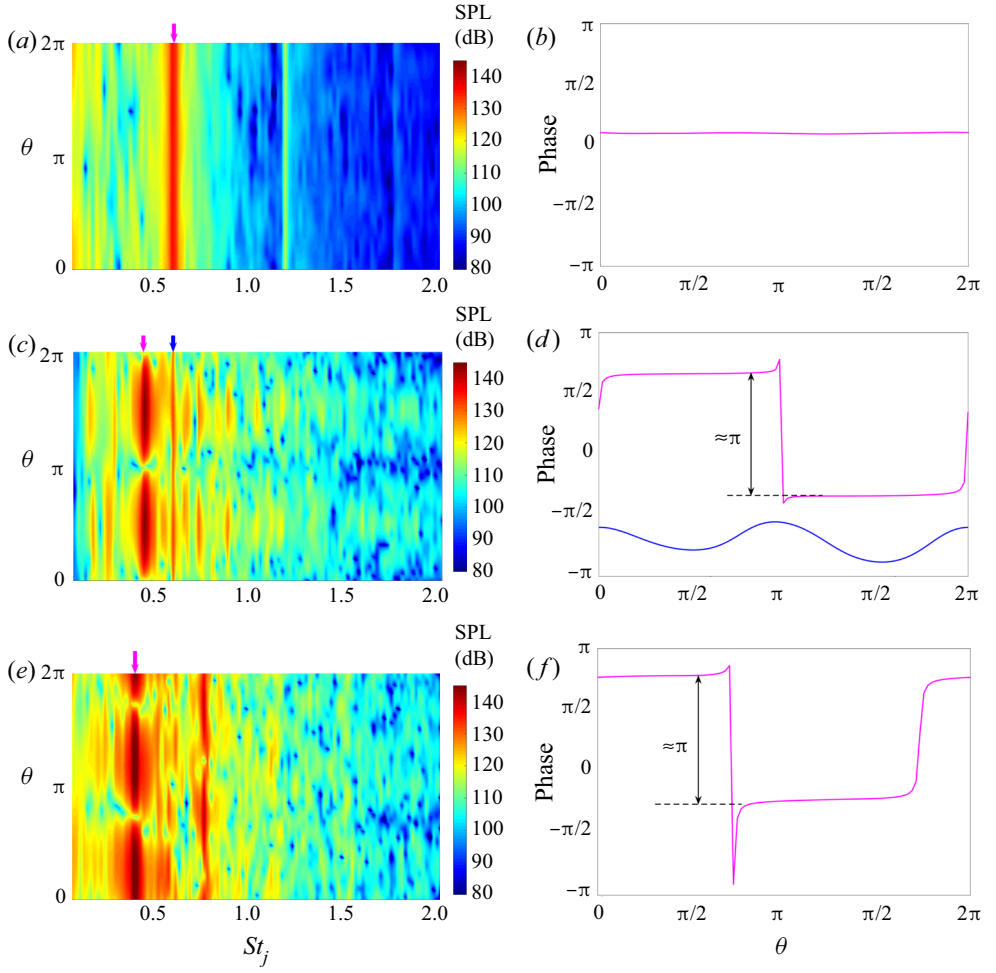

FIGURE 5. Noise spectra (*a*,*c*,*e*) and phase distributions (*b*,*d*,*f*) of screech tones along the circular line $(x, r) = (0, 2)$ for the jet at NPR = 2.2 (*a*,*b*), NPR = 2.4 (*c*,*d*) and NPR = 2.6 (*e*,*f*). The colours of the arrows in (*a*,*c*,*e*) correspond to the colours of the curves in (*b*,*d*,*f*).

less than π. The extreme value points on the phase curve are near $\theta = 0$ and π where the phase of the screech tone at $St_j = 0.4237$ jumps. It can be inferred that the screech tone at $St_j = 0.5778$ is at an axisymmetric mode, but becomes a little tilted under the influence of the flapping mode. For the jet at the NPR of 2.6, in figure 5(*e*), there is a screech tone at $St_j = 0.3743$ (the magenta arrow) that has variable amplitudes along the circular line of $(x, r) = (0, 2)$. And as shown in figure 5(*f*), the phase of this tone also abruptly changes leading to a phase difference of π. Thus, this screech tone is also at a flapping mode.

The acoustic wavelengths of the screech tones are calculated based on the screech frequencies and the ambient sound velocity. Figure 6 shows the comparisons of the acoustic wavelengths obtained from the present numerical simulations and the experiments of Ponton & Seiner (1992). The acoustic wavelengths shown in figure 6 are non-dimensionalized by the nozzle exit diameter D. The steady increase of the acoustic wavelength with the increasing ideally expanded Mach number M_j is segmented into several stages corresponding to the different instability modes of the jets. As shown in

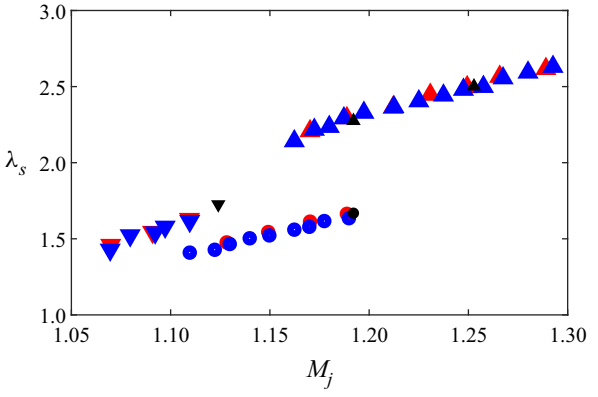

FIGURE 6. The comparisons of screech tone acoustic wavelengths between the experiments of Ponton & Seiner (1992) (red, ▼ = A1, ○ = A2 and ▲ = B modes for the nozzle with the lip of $0.2D$; blue, ▼ = A1, ○ = A2 and ▲ = B modes for the nozzle with the lip of $0.4D$); and the present numerical simulations (black, ▼ = A1, ○ = A2 and ▲ = B modes). M_j is the ideally expanded Mach number.

NPR/M_j	Screech mode	St_j
2.2/1.1240	A1	0.5804
2.4/1.1921	A2	0.5778
2.4/1.1921	B	0.4237
2.6/1.2528	B	0.3743

TABLE 3. The modes and Strouhal numbers of the screech tones; M_j is the ideally expanded Mach number.

figure 6, at the NPR of 2.2 ($M_j = 1.1240$), the acoustic wavelength of the screech tone falls on the extension of the curve for the A1 mode. For the jet at the NPR of 2.4 ($M_j = 1.1921$), the acoustic wavelengths of screech tones are located at the curves for the A2 and B mode, respectively. And at the NPR of 2.6 ($M_j = 1.2528$), the acoustic wavelength also has a good agreement with the experimental results at the B mode. Powell *et al*. (1992) demonstrated that the A1 and A2 modes are two toroidal modes and the B mode is a flapping mode. The characteristics of these modes agree well with the features of the screech tones that are shown in figure 5. Hu & McLaughlin (1990) suggested that the fine-scale turbulence is extraneous to the basic screech phenomenon. In their experiments, the screech frequencies of low-Reynolds-number jets agree well with their high-Reynolds-number counterparts. The present numerical simulations are conducted on jets with a low Reynolds number and the numerical results are also in good agreement with the experimental data. On the other hand, the good agreement between numerical and experimental results also demonstrates the accuracy of the present simulations. The modes and frequencies of the screech tones in the present simulations are summarized in table 3.

At the NPR of 2.4, two screech tones are presented in figure 5(*c*). However, Fourier analysis cannot reveal whether these two modes are coexisting or switching in a mutually exclusive fashion. Here we investigate the dynamic characteristics of screech tones via the

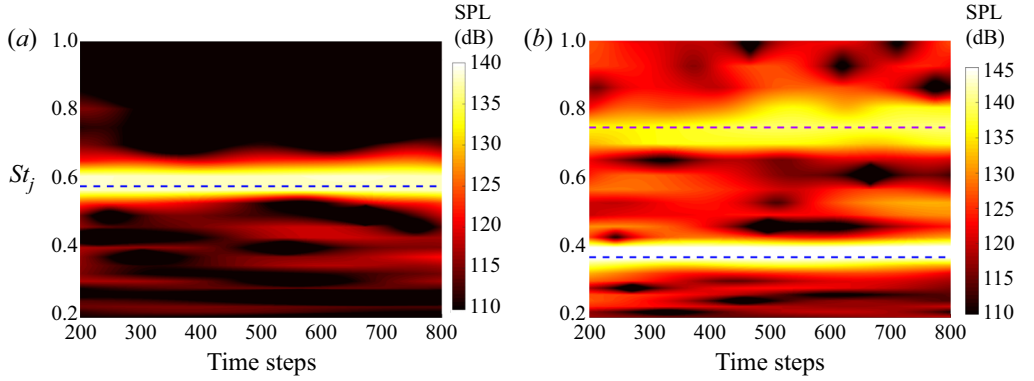

FIGURE 7. Time–frequency scalograms: (*a*) for the NPR = 2.2 jet, at $(x, \theta, r) = (0, \pi/2, 2)$, the blue dashed line corresponds to $St_j = 0.5804$; (*b*) for the NPR = 2.6 jet, at $(x, \theta, r) = (0, \pi/2, 2)$, the blue dashed line corresponds to $St_j = 0.3743$ and the purple dashed line corresponds to $St_j = 0.749$.

continuous wavelet transform (CWT) (Mancinelli *et al*. 2017, 2019). The wavelet transform is performed on the fluctuating pressure signal. The detailed process of the CWT is given by Mancinelli *et al*. (2017). The bump wavelet kernel is used here. The present CWT analyses are carried out by using the Matlab® software.

The fluctuating pressure is obtained at 1000 instants from the numerical simulations. Because of the edge effect of the CWT, the results from the 200th to the 800th stored instants are shown. Firstly, the CWT analyses are conducted on the pressure fluctuations at a point in the nozzle exit plane for the jets at the NPRs of 2.2 and 2.6. The results are shown in figure 7(*a*,*b*), respectively. The screech frequencies and amplitudes for these two jets can remain stable in the time range of the numerical simulations. This demonstrates that the numerical simulations conducted on these two jets have reached stable states. Each screech tone corresponds to a high-amplitude band in figure 7. However, the current results are able to display the time evolutions of the screech frequencies and amplitudes.

Figure 8 shows the CWT results for the jet at the NPR of 2.4. At the point $(x, \theta, r) = (0, \pi, 2)$, only the screech tone at the A2 mode (the purple dashed line) is detected in figure 8(*a*). However, at the point $(x, \theta, r) = (0, 3\pi/2, 2)$, the screech tone at the A2 mode (the purple dashed line) and the B mode (the blue dashed line) can coexist steadily in figure 8(*b*). Furthermore, the CWT is applied on the fluctuating pressure in the jet shear layer. As shown in figure 9, at the azimuthal angle of $3\pi/2$, the instability waves at the B mode have a higher amplitude. The frequencies and amplitudes of the instability waves at the A2 and B modes are stable. Based on the above analyses, it can be concluded that the A2 and B modes can coexist in the jet at the NPR of 2.4. The screech tone at the B mode possessing a higher amplitude is dominant.

3.4. *Fourier decomposition of the pressure field*

The amplitude and phase fields of pressure fluctuations at the screech frequencies are obtained by Fourier transforms. As shown in figure 10(*a–d*), the amplitude fields in the (x, r) planes exhibit several cell structures along the jet boundary. These structures are standing waves, which have been observed previously in supersonic screeching jets experimentally by Panda (1999) and numerically by Gojon & Bogey (2017). Panda (1999) suggested that this standing wave pattern is formed by the interference

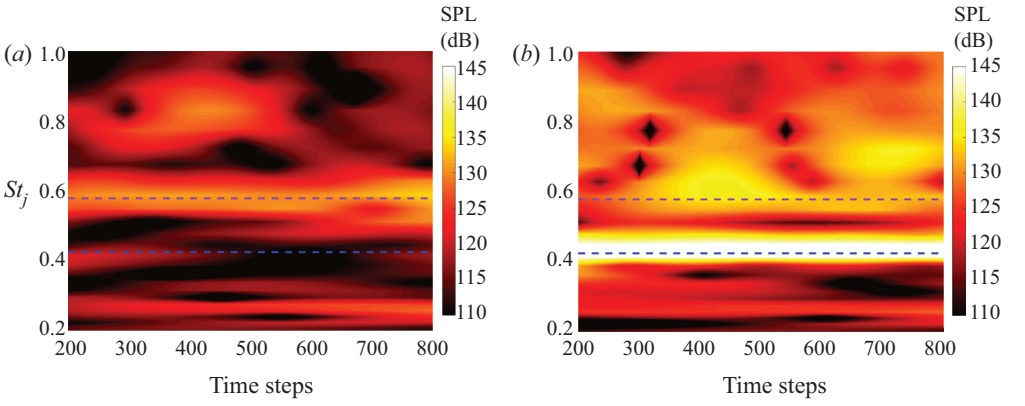

FIGURE 8. Time–frequency scalograms for the NPR = 2.4 jet: (*a*) at $(x, \theta, r) = (0, \pi, 2)$ and (*b*) at $(x, \theta, r) = (0, 3\pi/2, 2)$. The purple dashed line corresponds to $St_j = 0.5778$, and the blue dashed line corresponds to $St_j = 0.4237$.

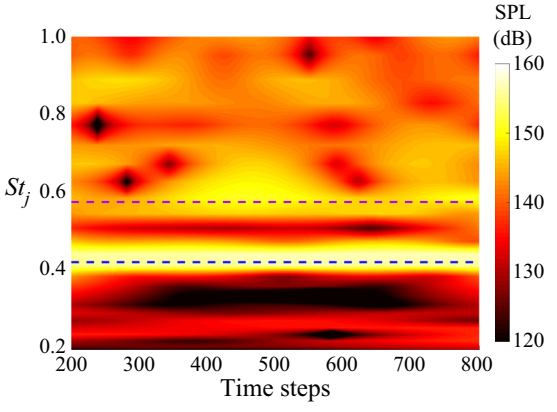

FIGURE 9. Time–frequency scalogram for the NPR = 2.4 jet at $(x, \theta, r) = (0.8, 3\pi/2, 0.5)$. The purple dashed line corresponds to $St_j = 0.5778$, and the blue dashed line corresponds to $St_j = 0.4237$.

between the downstream-propagating instability waves and the upstream-propagating acoustic fluctuations. The wavenumber of the standing wave k_{sw} can be calculated as

$$k_{sw} = k_a + k_h, \tag{3.3}$$

where k_a and k_h are, respectively, the wavenumbers of the upstream-propagating acoustic waves and the downstream-propagating instability waves (Panda 1999).

Detailed information about the spatial organizations of the pressure fields at the screech frequencies is revealed by the phase fields in the (x, r) planes and the nozzle exit plane. For the jet at the NPR of 2.2, the phase field at the screech frequency is symmetrical to the jet axis in figure 10(*e*), and is shown as an axisymmetric annular distribution in figure 11(*e*). Moreover, as shown in figure 11(*a*), the amplitudes at different azimuthal angles are nearly equivalent near the nozzle. These results further confirm that the screech tone of the jet at the NPR of 2.2 is at the axisymmetric A1 mode. Similar results are also found in figures 10(*f*), 11(*b*) and 11(*f*) for the screech tone at the NPR of 2.4 and $St_j = 0.5778$,

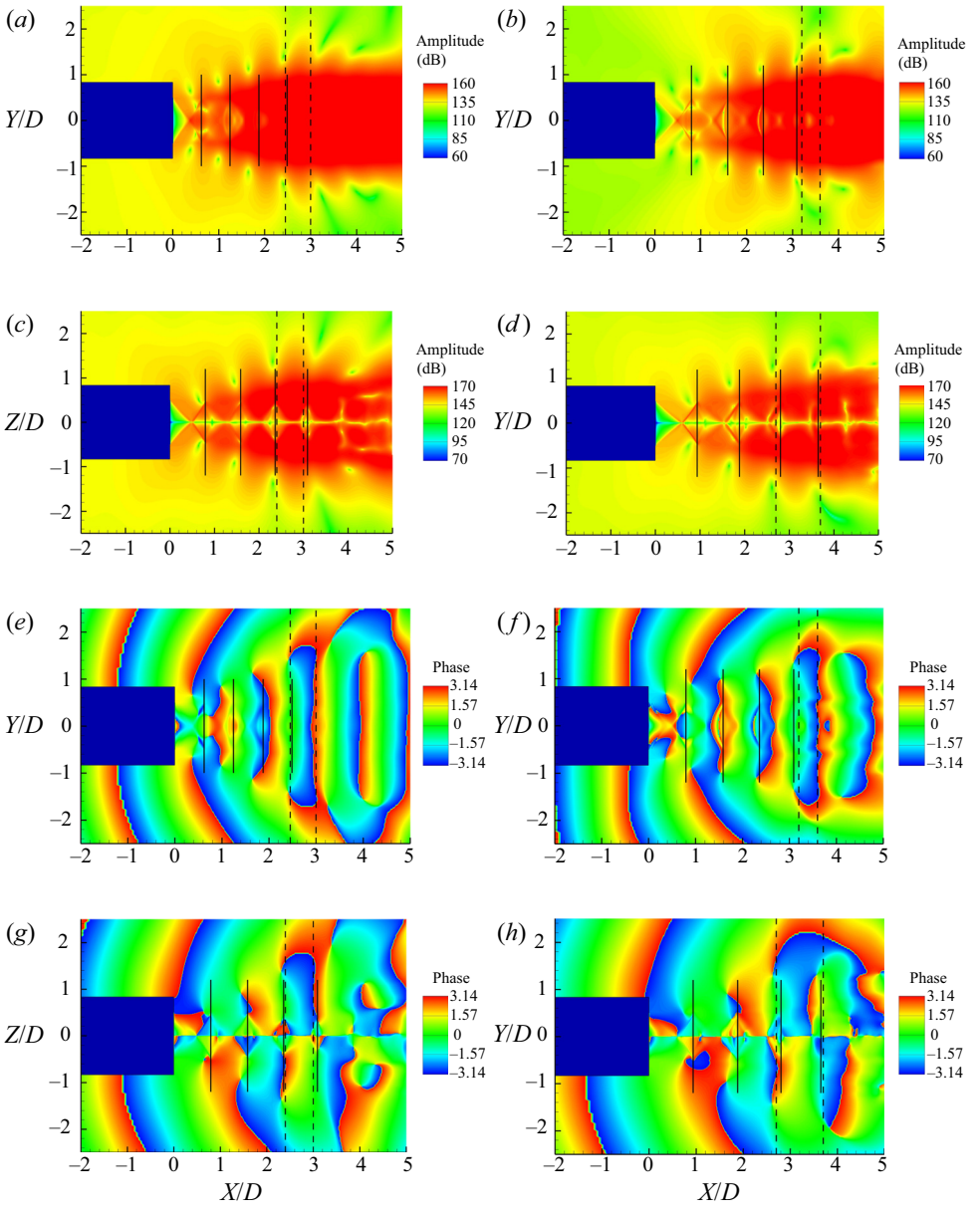

FIGURE 10. Amplitude (*a–d*) and phase (*e–h*) fields obtained in the (x, r) planes for the pressure fluctuations at screech frequencies: (*a*,*e*) NPR = 2.2 and $St_j = 0.5804$; (*b*,*f*) NPR = 2.4 and $St_j = 0.5778$; (*c*,*g*) NPR = 2.4 and $St_j = 0.4237$; (*d*,*h*) NPR = 2.6 and $St_j = 0.3743$. The dashed black lines mark the axial ranges of the effective sources. The black solid lines indicate the axial positions of the shock reflection points at the jet shear layer.

and confirm that this tone is at the axisymmetric A2 mode. As for the screech tone at the NPR of 2.4 and $St_j = 0.4237$, the phase field appears antisymmetric with respect to the jet axis in figure 10(*g*) and to the line $\theta = 0$ and π in figure 11(*g*), respectively. The azimuthal directivity of this screech tone is shown in figure 11(*c*). The radiation pattern resembling that of an acoustic dipole is characteristic of a flapping screech mode (Shen

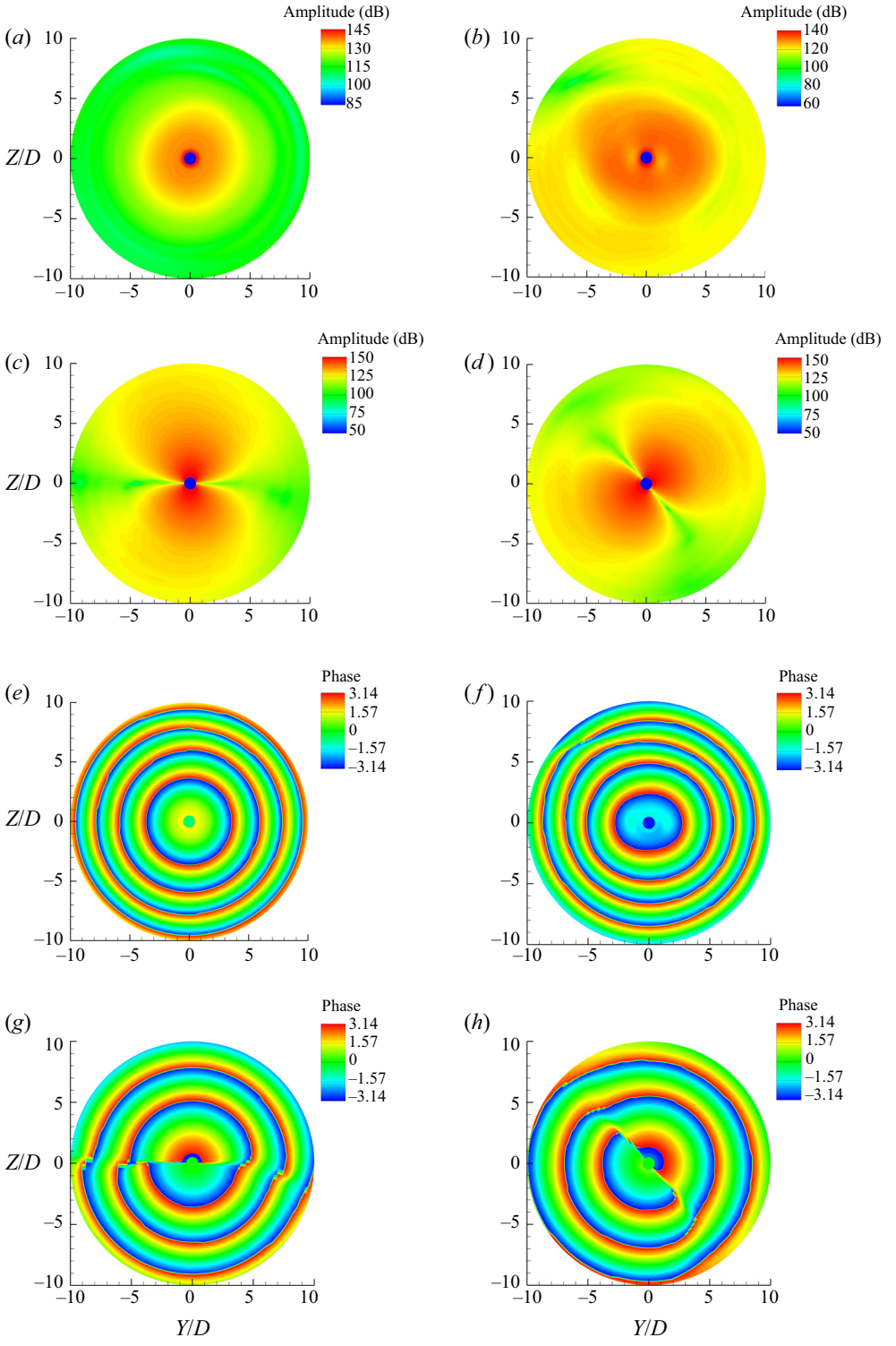

FIGURE 11. Amplitude (*a–d*) and phase (*e–h*) fields obtained in the nozzle exit plane for the pressure fluctuations at screech frequencies: (*a*,*e*) NPR = 2.2 and $St_j = 0.5804$; (*b*,*f*) NPR = 2.4 and $St_j = 0.5778$; (*c*,*g*) NPR = 2.4 and $St_j = 0.4237$; (*d*,*h*) NPR = 2.6 and $St_j = 0.3743$.

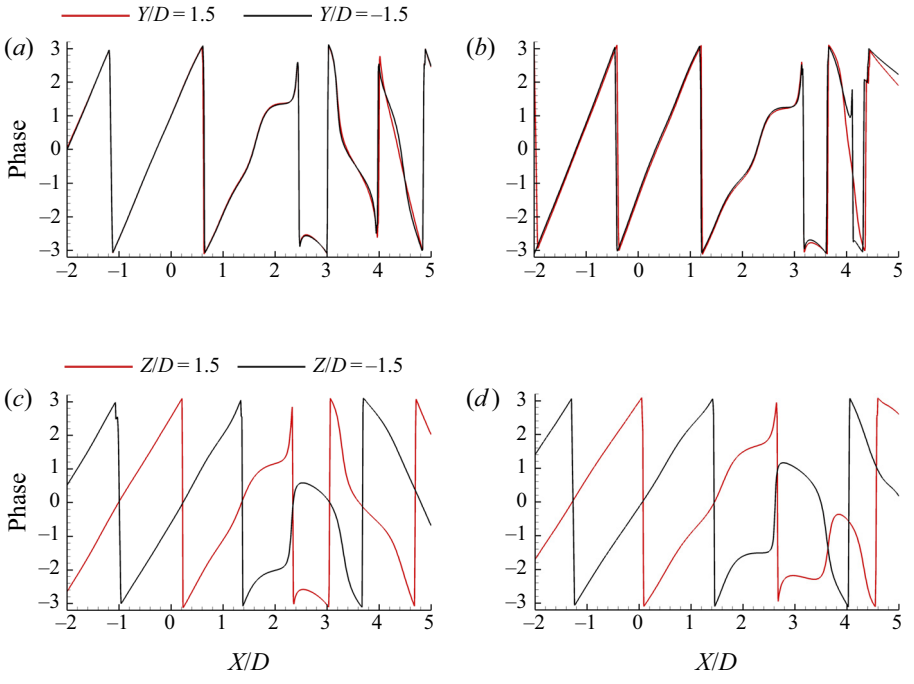

FIGURE 12. The distributions of the phase along the line $r = 1.5$ in figure 10(*e–h*): (*a*) corresponds to figure 10(*e*), (*b*) corresponds to figure 10(*f*), (*c*) corresponds to figure 10(*g*), and (*d*) corresponds to figure 10(*h*).

& Tam 2002). At the NPR of 2.6, as shown in figures 10(*h*), 11(*d*) and 11(*h*), the phase and amplitude fields of the screech tone at $St_j = 0.3743$ also display the characteristics of a flapping screech mode. For the two screech tones at the B mode, different azimuthal directivity angles can be observed in figure 11(*c*,*d*). The azimuthal directivity angle for a screech tone at the B mode is in a random fashion.

To determine the effective source locations for different screech tones, the distributions of the phase along the line $r = 1.5$ in figure 10(*e–h*) are shown in figure 12. Except for some discontinuity points, the sign of the slope of the phase changes around a range of axial positions in different cases. The slope of the phase is inversely proportional to the phase velocity of the wave projected onto the line. The inversion of the sign of the slope implies the inversion of the propagation direction of the wave (Mercier *et al*. 2017). In the present study, at upstream regions, the sign of the slope is positive and the wave propagates upstream. At downstream locations, the sign of the slope is negative and the wave propagates downstream. Therefore, the effective sources of the screech tones can be determined by figure 12. The effective source locations are at $X/D = 2.5 \sim 3$ for the A1 mode at the NPR of 2.2, at $X/D = 3.2 \sim 3.6$ for the A2 mode at the NPR of 2.4, at $X/D = 2.4 \sim 3$ for the B mode at the NPR of 2.4 and at $X/D = 2.7 \sim 3.6$ for the B mode at the NPR of 2.6. The ranges of the effective sources are marked in figure 10. The effective sources of the screech tones are located downstream of the fourth shock cell at the A1 and A2 modes and downstream of the third shock cell at the B mode.

For supersonic impinging jets, the acoustic feedback loop is established between the nozzle exit and the impinging plate. By considering the two semi-cells near the nozzle

NPR	Screech mode	N_p	N_{shock}
2.2	A1	4	4
2.4	A2	5	4
2.4	B	3	3
2.6	B	3	3

TABLE 4. The characteristics of the screech feedback loops: N_p is the number of periods contained in the feedback loop; N_{shock} is the number of shock cells between the nozzle and the effective source.

and the plate as one cell, the structures of hydrodynamic–acoustic standing waves contain a whole number of cells N_{sw} (Bogey & Gojon 2017). Gojon, Bogey & Marsden (2016) demonstrated that N_{sw} is also the number of periods N_p contained in the feedback loop. Here, for supersonic free jets, we consider that there are two semi-cells near the nozzle and the effective source location. The number of standing wave cells, namely the number of periods contained in the screech feedback loop, can be determined from figure 10(*a–d*). For the A1 mode, four periods are contained in the feedback loop, the A2 mode contains five periods and there are three periods in the feedback loop at the B mode. These results are in good agreement with the experimental results of Mercier *et al*. (2017). The characteristics of the screech feedback loops are summarized in table 4.

3.5. *Velocity spectra*

Figure 13 shows the power spectral densities (PSD) of the axial velocity fluctuations on the lip line ($r = 0.5$) at three axial positions. These spectra are azimuthally averaged. The first location of $X/D = 3$ is near or in the regions of the effective sources of the screech tones, and several peaks corresponding to the screech tones and their second harmonics can be observed. As shown in figure 13(*a*), for the jet at the NPR of 2.2, the peaks at $St_j = 0.5804$ (the magenta arrow) and 1.18 (the green arrow) are associated with the screech tone at the A1 mode and its second harmonic, respectively. And a plateau centred around $St_j = 0.29$ (the blue arrow), which is related to the subharmonic of the screech tone, also appears. For the jet at the NPR of 2.4, the peaks at $St_j = 0.4237$ (the magenta arrow) and 0.5778 (the blue arrow), which are respectively associated with the screech tones at the B and A2 modes and the peak at $St_j = 0.86$ (the green arrow) corresponding to the second harmonic at the B mode, are observed in figure 13(*b*). Because of the coexistence of these two screech modes, two humps around $St_j = 0.15$ (the frequency difference between the screech tones at the A2 and B modes, the cyan arrow) and $St_j = 0.28$ (the frequency difference between the screech tone at the A2 mode and the second harmonic at the B mode, the red arrow) also appear in figure 13(*b*). And at the NPR of 2.6, the peaks corresponding to the screech tone ($St_j = 0.3743$, the magenta arrow) and the second harmonic ($St_j = 0.749$, the blue arrow) can be observed in figure 13(*c*).

At the second axial position of $X/D = 7$, the velocity spectra are shown as broadband curves. The plateau around $St_j = 0.29$ is still visible for the jet at the NPR of 2.2 in figure 13(*a*). As shown in figure 13(*b*,*c*), because of the laminar-to-turbulent transition, a range of the spectra follows the $-5/3$ slope for the jets at the NPRs of 2.4 and 2.6. These results correspond to the more complex vortical structures at this axial position in

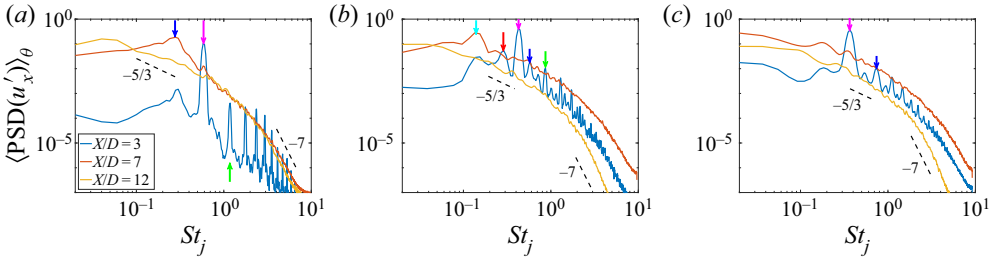

FIGURE 13. The power spectral densities (PSD) of non-dimensional axial velocity fluctuations u_x' at $X/D = 3$, 7 and 12 as a function of St_j: (*a*) NPR = 2.2, (*b*) NPR = 2.4 and (*c*) NPR = 2.6.

figure 2(*b*,*c*). The screech tone is produced by the growth of the natural jet instability, and the jet mixing can be enhanced by the feedback loop (Raman 1998). The enhancement of mixing depends on the mode and amplitude of the screech tone (Glass 1968; Raman 1998). In the present numerical simulations, for the jets at the NPRs of 2.4 and 2.6, the dominated screech tones are at the B mode and with higher amplitudes than the tones at the A1 and A2 modes. Therefore, the jets at the NPRs of 2.4 and 2.6 transit into turbulence earlier than the jet at the NPR of 2.2.

At a further downstream location of $X/D = 12$, we can observe that a range follows the $-5/3$ slope and a range follows the -7 slope in the spectra for all of the jets. This result agrees with the theoretical analyses of Batchelor (1953) and Heisenberg (1985), and demonstrates that, at this location, the flow has already transited into turbulence and, in the present numerical simulations, the inertial subregion and the viscous subrange of the turbulence have been resolved.

3.6. *Convection velocity*

The convection velocity of the instability waves in the shear layer is an important parameter of the screech feedback loop. The screech frequencies at different modes have already been obtained. The averaged convection velocity is determined as

$$\overline{U_c} = \frac{\omega_s}{k_h}, \tag{3.4}$$

where ω_s is the angular frequency of the screech tone. In § 3.4, Fourier transforms have been conducted on pressure fluctuations and the Fourier coefficients at the screech frequencies are obtained. The wavenumbers k_h are determined by one-dimensional spatial Fourier transforms that are performed on the Fourier coefficients at the screech frequencies. The spatial Fourier transforms are conducted along the axial line of $r = 0.6$ and in the region of $0 \leq x \leq 4$ that covers the effective sources. The results are shown in figure 14. The maximum peaks are marked by the blue dashed lines in figure 14 and the corresponding wavenumbers are collected in table 5 as $k_h D_j$. The averaged convective velocity is calculated by (3.4). The convective Mach numbers $M_c = \overline{U_c}/a_\infty$ are shown in table 5 and range from 0.55 to 0.65. The wavenumbers corresponding to the upstream-propagating acoustic waves $k^- = -\omega_s/a_\infty$ are represented by red dashed lines in figure 14. In each wavenumber spectrum, the central wavenumber of the highest bump in the negative wavenumber range has a good agreement with k^-. It indicates that this bump is related to the upstream-propagating acoustic wave.

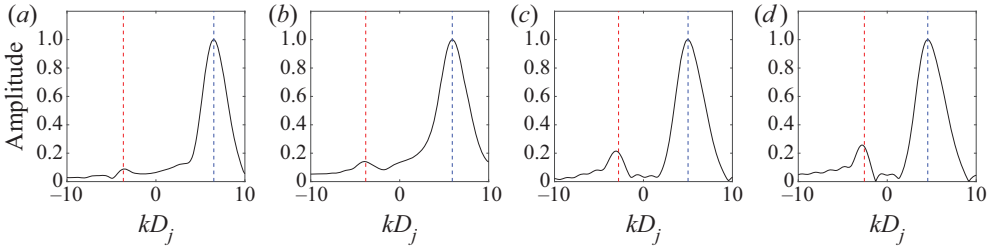

FIGURE 14. Normalized wavenumber spectra at screech frequencies: (*a*) NPR = 2.2 and St_j = 0.5804, (*b*) NPR = 2.4 and $St_j = 0.5778$, (*c*) NPR = 2.4 and $St_j = 0.4237$, and (*d*) NPR = 2.6 and $St_j = 0.3743$. The wavenumbers of $k^- = -\omega_s/a_\infty$ are indicated by the vertical red dashed lines. The peaks in positive wavenumber range are indicated by the vertical blue dashed lines.

NPR	Screech mode	$k_h D_j$	M_c
2.2	A1	6.51	0.563
2.4	A2	5.91	0.646
2.4	B	5.01	0.559
2.6	B	4.56	0.564

TABLE 5. The wavenumber and convective Mach number of the instability waves.

4. Aeroacoustic feedback model

4.1. *Classical feedback model*

The screech tone of underexpanded free jets is due to an acoustic feedback loop, which was described in Powell (1953) and Tam (1995). This feedback mechanism establishes between the nozzle lip and the effective source. The instability waves in the jet shear layer interact with shocks around the effective source and the upstream-propagating feedback acoustic waves are produced. The feedback acoustic waves propagate to the nozzle exit outside the jet, excite the shear layer and close the feedback loop. Based on this classical feedback model, the non-dimensional screech frequency f_s can be predicted as (Powell 1953)

$$f_s = \frac{M_c}{\lambda_{sh}(1 + M_c)}, \tag{4.1}$$

where λ_{sh} is the spacing of the shock cell non-dimensionalized by the nozzle exit diameter D. To account for the staging behaviour of the screech tone, Gao & Li (2010) characterized each mode by the parameters N_p and N_{shock}, and proposed a modification of (4.1):

$$f_s = \frac{N_p M_c}{N_{shock}\lambda_{sh}(1 + M_c)}. \tag{4.2}$$

Screech frequencies are estimated by (4.2) based on the parameters given in tables 4 and 5. The spacing of the first shock cell λ_1 determined numerically in table 2 is used to approximate the spacing of the shock cell in (4.2). In table 6, these estimated screech frequencies are compared with the screech frequencies that are obtained from the numerical simulations. The screech frequencies estimated by the classical feedback model are in good agreement with the numerical results. However, the coexistence of the screech tones at the A2 and B modes cannot be explained by the feedback model reported

NPR	Screech mode	St_j (given in table 2)	St_j (calculated by (4.2))	Relative error (%)
2.2	A1	0.5804	0.5820	0.3
2.4	A2	0.5778	0.5986	3.6
2.4	B	0.4237	0.4375	3.3
2.6	B	0.3743	0.3632	3.0

TABLE 6. Comparison of screech frequencies obtained from the numerical simulations and estimated by equation (4.2).

above. For that reason, an alternative feedback model, which is associated with the upstream-propagating acoustic wave mode of the jet (Tam & Ahuja 1990), is considered in the following section.

4.2. *Combination of the feedback model and the upstream-propagating acoustic modes of the jets*

The upstream-propagating neutral acoustic wave modes of high-speed jets were first identified by Tam & Hu (1989). In the feedback models proposed by Tam & Ahuja (1990) and Tam & Norum (1992), the feedback loops in subsonic round impinging jets and supersonic rectangular impinging jets are closed by the waves belonging to the upstream-propagating acoustic modes of the jets. Recently, these acoustic modes have been detected in the potential core of subsonic free jets by Towne *et al*. (2017) and in supersonic impinging jets by Gojon *et al*. (2016) and Bogey & Gojon (2017). Some evidence also demonstrates that the screech feedback loops in supersonic free jets are closed by the neutral acoustic wave modes (Edgington-Mitchell *et al*. 2018; Gojon *et al*. 2018; Mancinelli *et al*. 2019).

The dispersion relation of the upstream-propagating neutral acoustic wave mode in a round jet was derived by Tam & Ahuja (1990). For the neutral acoustic wave modes considered here, both the axial wavenumber k and angular frequency ω are real numbers. The dispersion relation can be written as

$$|\xi_+|J_n(|\xi_-\alpha|)\frac{K_{n-1}(|\xi_+\alpha|)+K_{n+1}(|\xi_+\alpha|)}{K_n(|\xi_+\alpha|)} + \frac{C^2|\xi_-|}{(a_\infty C/a_j-M_j)^2}[J_{n-1}(|\xi_-\alpha|)-J_{n+1}(|\xi_-\alpha|)]=0, \tag{4.3}$$

where a_∞ and a_j are the sound speeds in the ambient and at the ideally expanded condition of the jet, $C=\omega/(ka_\infty)$, J_n is the nth-order Bessel function of the first kind, $\xi_+ = |C^2-1|^{1/2}$, $\xi_- = |(a_\infty C/a_j - M_j)^2-1|^{1/2}$, $\alpha = kD_j/2$ and K_n is the nth-order modified Bessel function. For the underexpanded jets in the present numerical simulations, the equivalent ideally expanded Mach number M_j and nozzle diameter D_j at different NPRs are given by

$$M_j=\sqrt{(\mathrm{NPR}^{(\gamma-1)/\gamma}-1)\frac{2}{\gamma-1}}, \quad \frac{D_j}{D}=\left[\frac{1+\frac{1}{2}(\gamma-1)M_j^2}{1+\frac{1}{2}(\gamma-1)M_e^2}\right]^{(\gamma+1)/4(\gamma-1)}\left(\frac{M_e}{M_j}\right)^{1/2}, \tag{4.4a,b}$$

where $\gamma=1.4$ and the exit Mach number $M_e=1$ for the convergent nozzle.

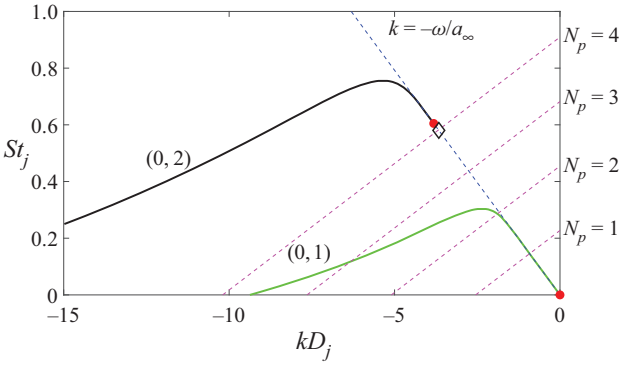

FIGURE 15. Representation of the dispersion relations of the axisymmetric neutral acoustic wave modes for an ideally expanded jet at $M_j = 1.1240$. The red dot indicates the lower limits of the modes; the magenta dotted lines show the relation (4.5) for the A1 mode at the NPR of 2.2; and the diamond marks the screech frequency at the A1 mode.

In order to combine the classical feedback model and the upstream-propagating acoustic wave mode of the jet, the wavenumber k_a of the upstream-propagating acoustic wave in the classical feedback loop is assumed to be equal to the opposite of the wavenumber k of the upstream-propagating acoustic wave mode (Gojon *et al.* 2016; Bogey & Gojon 2017). By considering that $k_{sw} = 2\pi N_{sw}/(N_{shock}\lambda_{sh})$, $N_{sw} = N_p$, $k_h = 2\pi f_s/M_c$ and $k_a = -k$, equation (3.3) yields

$$f_s = \frac{N_p M_c}{N_{shock}\lambda_{sh}} + \frac{kM_c}{2\pi}. \tag{4.5}$$

The solutions of this equation are dependent on the location of the effective source and the averaged convection Mach number.

For each α and azimuthal wavenumber n, the dispersion relation (4.3) has many eigenvalues that can be ordered according to their radial wavenumber m (Tam & Hu 1989). In what follows, the acoustic mode that corresponds to the azimuthal wavenumber n and the radial wavenumber m will be denoted by (n, m) for convenience.

In figure 15, the dispersion relations of the axisymmetric acoustic wave modes for the ideally expanded jet at $M_j = 1.1240$ and the solutions of the feedback model (4.5) for the A1 mode at the NPR of 2.2 are shown as functions of the Strouhal number and the axial wavenumber. The screech tone at $St_j = 0.5804$ is also indicated on the line $k = -\omega/a_\infty$. As shown in figure 15, the screech tone is located at the intersection of the line $k = -\omega/a_\infty$ and the line of equation (4.5) at $N_p = 4$, and just below the curve of the (0, 2) mode. The small discrepancy may be due to the presence of shocks in the simulated jet (Gojon *et al.* 2018) and the hypothesis of an inviscid infinitely thin shear layer in the vortex sheet model (Tam & Ahuja 1990). In the same way, the results of the axisymmetric acoustic wave modes for the ideally expanded jet at $M_j = 1.1921$ and the feedback model (4.5) for the A2 mode at the NPR of 2.4 are shown in figure 16. The screech tone at $St_j = 0.5778$ is very close to the intersection of the curve of the (0, 2) mode and the line of the feedback model (4.5) with $N_p = 5$. The above results are in agreement with the properties of the screech feedback loop summarized in table 4 and indicate that the screech tones at the A1 and A2 modes are generated by the feedback loops that are closed by the upstream-propagating (0, 2) mode of the equivalent ideally expanded jets. This conclusion agrees with the results of Edgington-Mitchell *et al.* (2018).

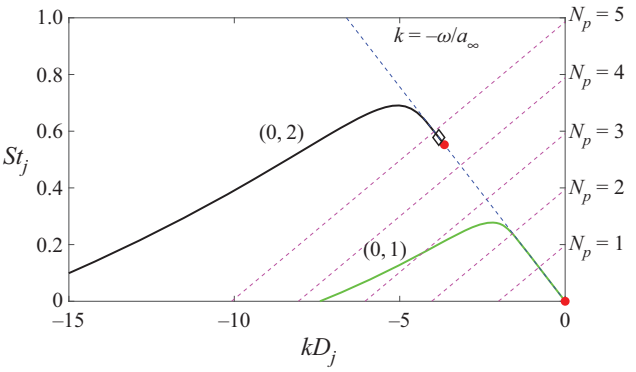

FIGURE 16. Representation of the dispersion relations of the axisymmetric neutral acoustic wave modes for an ideally expanded jet at $M_j = 1.1921$. The red dot indicates the lower limits of the modes; the magenta dotted lines show the relation (4.5) for the A2 mode at the NPR of 2.4; and the diamond marks the screech frequency at the A2 mode.

The screech frequencies at the A1 and A2 modes are located just above or below the lower limit of the (0, 2) mode. As shown by the dispersion curves in figures 15 and 16, the group velocities and phase velocities of the waves near the lower limit of the (0, 2) mode are very close to $-a_\infty$. It indicates that the upstream-propagating waves that close the feedback loop should propagate at a speed that is nearly equal to $-a_\infty$. This is also one requirement of the classical feedback model (4.2).

The flapping B mode can be modelled by two oppositely rotating helical modes that have the same amplitude (Powell *et al*. 1992; Ponton & Seiner 1995). Thus, the relation between the screech frequencies at the B mode and the helical ($n = 1$) upstream-propagating acoustic wave modes are examined here. The results of the model combination for the jet at the NPR of 2.4 and the screech tone at the B mode are shown in figure 17. The screech tone at $St_j = 0.4237$ is located at the intersection of the line $k = -\omega/a_\infty$ and the line of equation (4.5) at $N_p = 3$, and below the curve of the (1, 1) mode. A similar result is shown in figure 18 for the jet at the NPR of 2.6 with a larger difference between the screech frequency and the lower limit of the (1, 1) mode. Thus, the modified feedback model combined with the helical acoustic mode fails to estimate the screech frequency at the B mode. The screech feedback loop is closed by the upstream-propagating free-stream acoustic waves at the B mode.

Based on the wavelet analysis in § 3.3, for the jet at the NPR of 2.4, the screech tones at the A2 and B modes can coexist. In the research of Mancinelli *et al*. (2019), the screech tones at the A1 and A2 modes for the underexpanded jet at $M_j = 1.125$ are mutually exclusive. The dispersion relations of the axisymmetric acoustic wave modes of the ideally expanded jet at $M_j = 1.125$ are shown in figure 19. The screech tones at $St_j = 0.63$ (A1 mode) and $St_j = 0.7$ (A2 mode) are obtained from Mancinelli *et al*. (2019) and labelled on the line $k = -\omega/a_0$. Both of the screech tones are located at the curve of the acoustic wave mode (0, 2). For the screech tones at the A1 and A2 modes, the (0, 2) mode is the upstream-propagating component of the feedback cycle. For the B mode, the feedback process is closed by the upstream-propagating free-stream acoustic waves. Different upstream-propagating components of the feedback loops result in the coexistence of the A2 and B modes. And the same upstream-propagating component of the feedback loop leads to the mutual exclusion between the screech tones at the A1 and A2 modes.

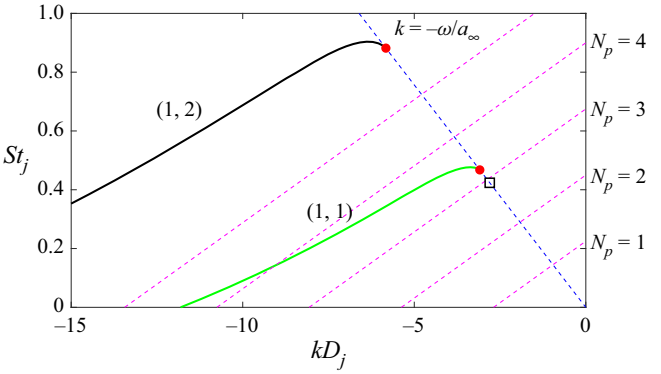

FIGURE 17. Representation of the dispersion relations of the helical neutral acoustic wave modes for an ideally expanded jet at $M_j = 1.1921$. The red dot indicates the lower limits of the modes; the magenta dotted lines show the relation (4.5) for the B mode at the NPR of 2.4; and the square marks the screech frequency at the B mode.

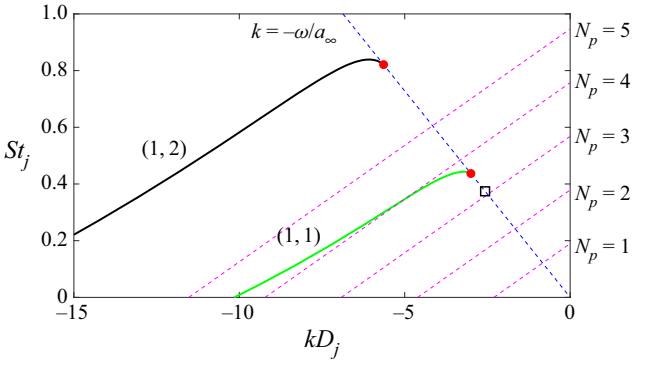

FIGURE 18. Representation of the dispersion relations of the helical neutral acoustic wave modes for an ideally expanded jet at $M_j = 1.2528$. The red dot indicates the lower limits of the modes; the magenta dotted lines show the relation (4.5) for the B mode at the NPR of 2.6; and the square marks the screech frequency at the B mode.

5. Dynamic mode decomposition

5.1. *The DMD algorithm*

Unsteady flows always exhibit complex flow structures, with a wide range of temporal and spatial features. Some modal analysis techniques, such as proper orthogonal decomposition (POD; Lumley 1967; Sirovich 1987) and dynamic mode decomposition (DMD; Schmid 2010), are used to extract the physically important coherent structures. The temporal coefficient of a spatial POD mode generally contains a mix of frequencies (Taira *et al*. 2017). DMD provides a method to decompose the time-resolved data that are obtained from numerical simulations or experiments into modes, with each mode having a single temporal frequency and growth/decay rate (Taira *et al*. 2017). Thus, the coherent flow structures associated with the screech tones are extracted by DMD in the present paper. The key steps of DMD (Schmid 2010) are outlined briefly in what follows.

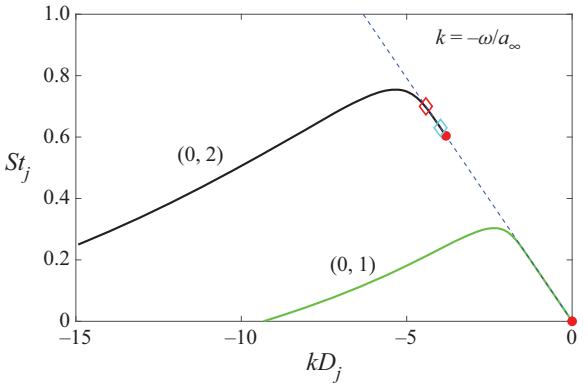

FIGURE 19. Representation of the dispersion relations of the axisymmetric neutral acoustic wave modes for an ideally expanded jet at $M_j = 1.125$. The red dot indicates the lower limits of the acoustic wave modes; the screech frequencies at the A1 mode (blue diamond) and A2 mode (red diamond) are obtained from Mancinelli *et al.* (2019).

The instantaneous data are represented in the form of a snapshot sequence, and two data matrices are given as

$$\boldsymbol{V}_1 = \{\boldsymbol{v}_0, \boldsymbol{v}_1, \boldsymbol{v}_2, \ldots, \boldsymbol{v}_{N-1}\}, \qquad \boldsymbol{V}_2 = \{\boldsymbol{v}_1, \boldsymbol{v}_2, \boldsymbol{v}_3, \ldots, \boldsymbol{v}_N\}, \tag{5.1a,b}$$

where $\boldsymbol{v}_i$ is the data sample at the ith temporal instant. We assume that a linear mapping $\boldsymbol{A}$ connects these two matrices, that is

$$\boldsymbol{V}_2 = \boldsymbol{A}\boldsymbol{V}_1. \tag{5.2}$$

A singular value decomposition on the data matrix $\boldsymbol{V}_1$ is performed,

$$\boldsymbol{V}_1 = \boldsymbol{U}\boldsymbol{\Sigma}\boldsymbol{W}^{\mathrm{H}}, \tag{5.3}$$

where the superscript 'H' denotes conjugate transpose. By combining the result of the singular value decomposition and (5.2), we obtain that

$$\boldsymbol{U}^{\mathrm{H}}\boldsymbol{A}\boldsymbol{U} = \boldsymbol{U}^{\mathrm{H}}\boldsymbol{V}_2\boldsymbol{W}\boldsymbol{\Sigma}^{-1} \equiv \tilde{\boldsymbol{S}}. \tag{5.4}$$

The DMD eigenvalues μ_i are obtained by solving the following eigenvalue problem:

$$\tilde{\boldsymbol{S}}\boldsymbol{y}_i = \mu_i \boldsymbol{y}_i. \tag{5.5}$$

And the DMD modes $\boldsymbol{\Phi}_i$ are obtained by

$$\boldsymbol{\Phi}_i = \boldsymbol{U}\boldsymbol{y}_i. \tag{5.6}$$

5.2. *DMD results*

In the present DMD, the instantaneous flow variables of the non-dimensional velocity components u_x, u_θ, u_r and pressure p are analysed simultaneously. The data from two-dimensional sections of the flow field constitute the data sample at each instant. The total number of snapshots is 501 and the non-dimensional time interval is 0.05.

NPR	Screech mode	St_j (given in table 2)	St_j (from DMD)	Planes
2.2	A1	0.5804	0.5882	$\theta = 0$ and π
2.4	A2	0.5778	0.5789	$\theta = 0$ and π
2.4	B	0.4237	0.4317	$\theta = \pi/2$ and $3\pi/2$
2.6	B	0.3743	0.3806	$\theta = 0$ and π

TABLE 7. Strouhal numbers of the chosen DMD modes.

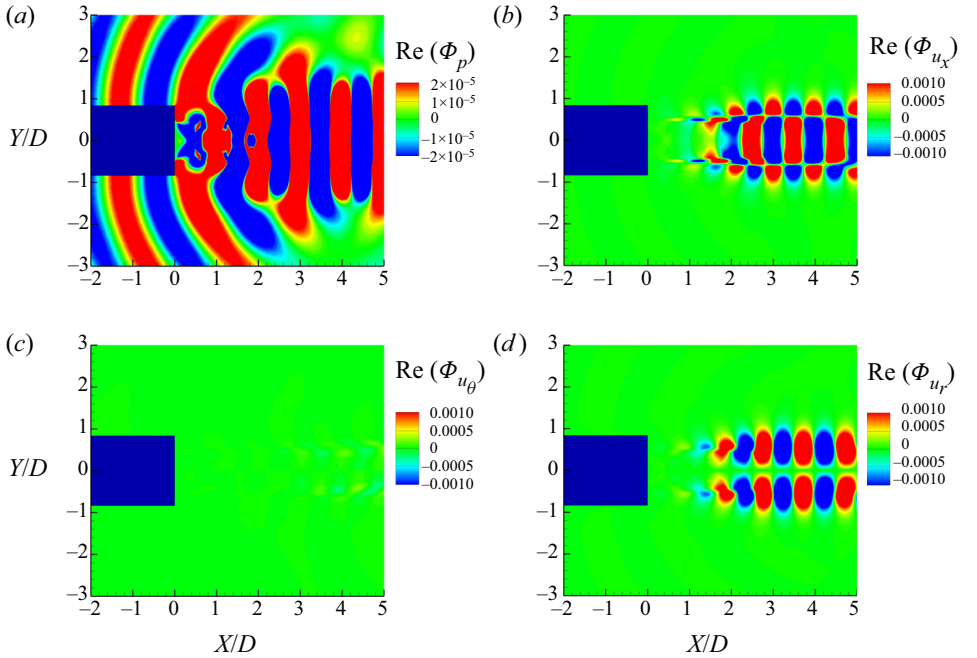

FIGURE 20. The real part of the DMD mode at $St_j = 0.5882$ for the NPR = 2.2 jet in the planes $\theta = 0$ and π: (*a*) the pressure component Φ_p, (*b*) the axial velocity component Φ_{u_x}, (*c*) the azimuthal velocity component Φ_{u_θ} and (*d*) the radial velocity component Φ_{u_r}.

At different NPRs, the screech frequencies are obtained by the Fourier transforms conducted on the fluctuating pressure in § 3.3. Thus, the DMD modes whose frequencies are nearest to the screech frequencies are chosen and analysed in detail. For different screech tones, the data in different azimuthal planes are processed by the DMD algorithm. The subdomain considered in the current DMD analyses extends from $x = -2$ to $x = 5$, which covers the effective source location at each screech mode. The frequencies of the chosen DMD modes are compared with the screech frequencies in table 7.

The DMD mode at $St_j = 0.5882$ for the jet at the NPR of 2.2 is shown in figure 20. The contour levels of the pressure component are adjusted to show the acoustic waves in the ambient of the jet. In figure 20(*a*), the upstream-propagating acoustic waves around the jet are observed and these waves are symmetric with respect to the jet axis. The symmetrical distributions of the axial and radial velocity components correspond to the axisymmetric vortices that are shown in figure 2(*a*). Moreover, there is nearly nothing shown in the

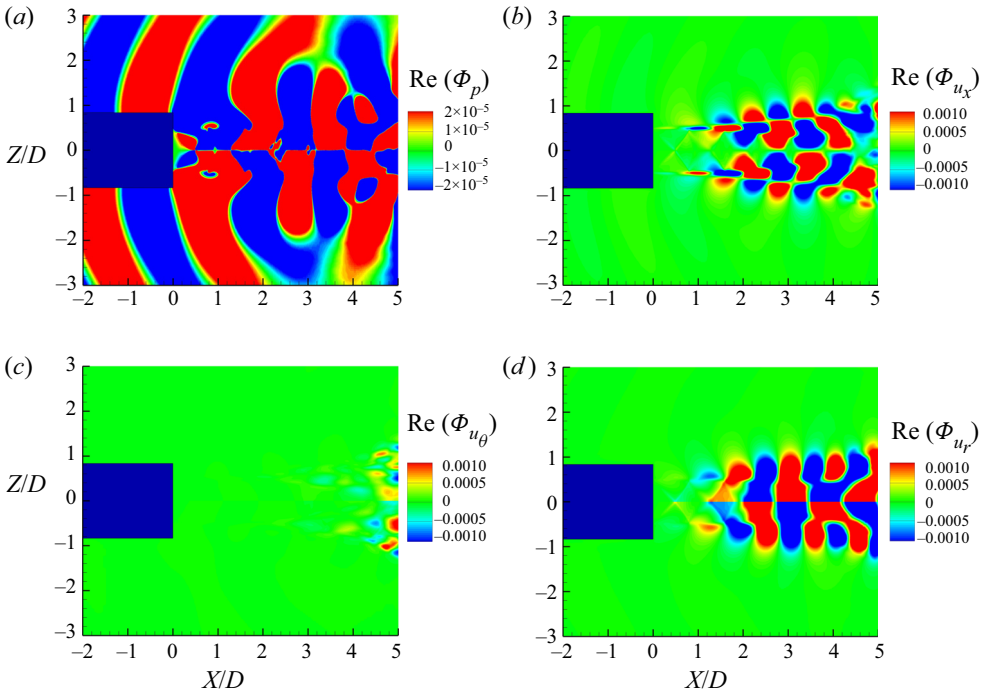

FIGURE 21. The real part of the DMD mode at $St_j = 0.4317$ for the NPR = 2.4 jet in the planes $\theta = \pi/2$ and $3\pi/2$: (*a*) the pressure component Φ_p, (*b*) the axial velocity component Φ_{u_x}, (*c*) the azimuthal velocity component Φ_{u_θ} and (*d*) the radial velocity component Φ_{u_r}.

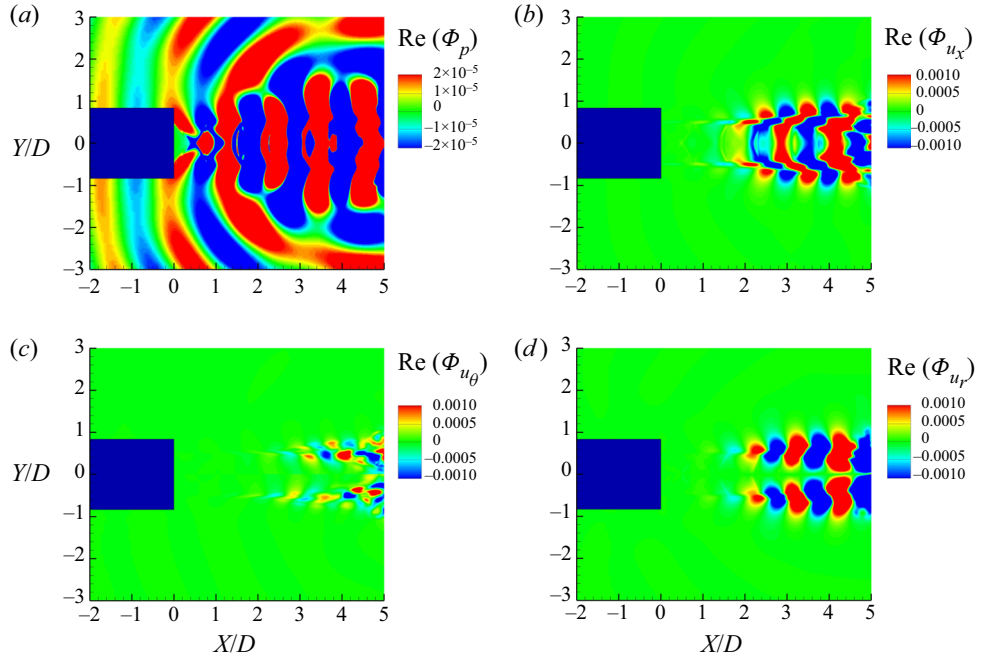

FIGURE 22. The real part of the DMD mode at $St_j = 0.5789$ for the NPR = 2.4 jet in the planes $\theta = 0$ and π: (*a*) the pressure component Φ_p, (*b*) the axial velocity component Φ_{u_x}, (*c*) the azimuthal velocity component Φ_{u_θ} and (*d*) the radial velocity component Φ_{u_r}.

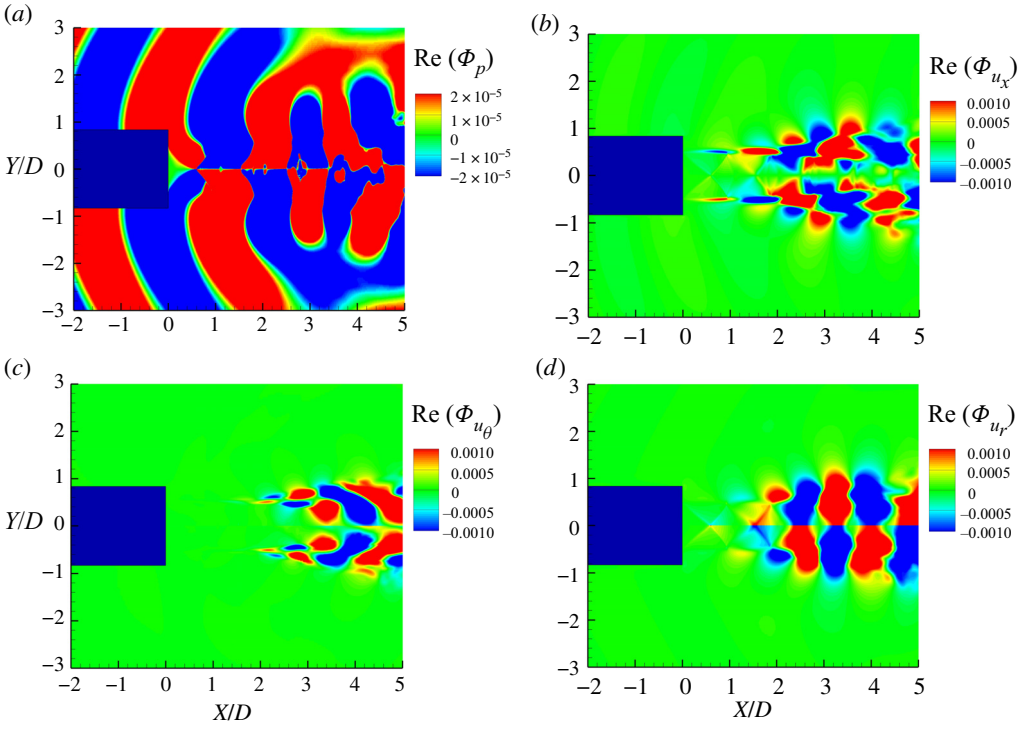

FIGURE 23. The real part of the DMD mode at $St_j = 0.3806$ for the NPR = 2.6 jet in the planes $\theta = 0$ and π: (*a*) the pressure component Φ_p, (*b*) the axial velocity component Φ_{u_x}, (*c*) the azimuthal velocity component Φ_{u_θ} and (*d*) the radial velocity component Φ_{u_r}.

azimuthal velocity component. These results indicate that the flow structures associated with the A1 mode are axisymmetric and have no observable azimuthal motions.

For the jet at the NPR of 2.4, the dominant screech tone is at the B mode. The DMD mode at $St_j = 0.4317$ is shown in figure 21. In figure 21(*a*), the upstream-propagating acoustic waves are out of phase relative to the jet axis. The antisymmetric patterns of the axial and radial velocity components in the jet shear layer correspond to the antisymmetric vortices that are shown in figure 2(*b*). And the flapping motions of the jet in the planes $\theta = \pi/2$ and $3\pi/2$ are also represented by the antisymmetric distribution of the radial velocity around the jet axis. As shown in figure 21(*c*), upstream of the effective source, there is nearly nothing displayed by the azimuthal velocity component. Because of the enhancement of the jet mixing, scattered distributions of the azimuthal velocity can be observed downstream of the effective source.

At the NPR of 2.4, the A2 and B modes are coexisting. The DMD mode at $St_j = 0.5789$ in the planes $\theta = 0$ and π is shown in figure 22. The symmetrical distributions of the pressure, axial velocity and radial velocity are observed in figure 22(*a*,*b*,*d*). These results represent the axisymmetric characteristics of the A2 mode. However, as shown in figure 22(*c*), the distribution of azimuthal velocity is nearly antisymmetric. The antisymmetric distribution of the azimuthal velocity is a representation of the motion that is vertical to the plane. By considering that the coherent structures associated with the B mode show a flapping motion in the planes $\theta = \pi/2$ and $3\pi/2$, which are vertical to the planes in figure 22, it can be concluded that the flow structures associated with the

A2 mode display a slight oscillation that is vertical to the planes $\theta = 0$ and π under the influence of the flow structures associated with the B mode.

As for the B mode of the jet at the NPR of 2.6, the DMD mode at $St_j = 0.3806$ in the planes $\theta = 0$ and π is shown in figure 23. As shown in figure 23(*a*,*b*,*d*), the distributions of the pressure, axial velocity and radial velocity are antisymmetric corresponding to the characteristics of the flapping B mode. As shown in figure 23(*d*), the in-plane flapping motions of the jet and the shock that is located at $x = 1.5 \sim 2$ are displayed by the antisymmetric distribution of the radial velocity near the jet axis. Furthermore, the symmetric distribution of the azimuthal velocity is observed in figure 23(*c*) and this is a representation of the rotational movement in the azimuthal direction.

6. Conclusion

In this paper, numerical simulations are conducted on the underexpanded free jets at the NPRs of 2.2, 2.4 and 2.6 and a Reynolds number of 2.5×10^3. The acoustic feedback loop responsible for the production of the screech tone and the staging process between the A2 and B modes are investigated.

At first, the main characteristics of the flow fields, such as the instantaneous flow structures and the shock cell spacings, are represented. The screech frequencies are obtained via the Fourier transforms conducted on the fluctuating pressure in the nozzle exit plane. The screech tone is at the A1 mode for the jet at the NPR of 2.2 and at the B mode for the jet at the NPR of 2.6. Two screech tones that are respectively at the A2 mode and the B mode are identified in the jet at the NPR of 2.4. The results of the wavelet analyses demonstrate that the screech tones at the A2 and B modes can coexist. The detailed spatial organization of the acoustic feedback loops is explored through the phase and amplitude fields at the screech frequencies. The numbers of shock cells between the nozzle exit and the effective sources are four for the A1 and A2 modes and three for the B mode. The number of periods contained in the feedback loop is equal to the number of cells in the standing wave pattern between the nozzle and the effective source. There are four periods for the A1 mode, five periods for the A2 mode and three periods for the B mode. The velocity spectra at different axial positions and the convection velocities of the instability waves are also obtained.

Secondly, based on the present numerical results, the classical feedback model which is closed by the acoustic waves travelling upstream outside the jet accurately estimates the screech frequencies at different modes. A modified model that combines the classical feedback model and the upstream-propagating acoustic wave mode of the equivalent ideally expanded jet is introduced. The $(0, 2)$ acoustic mode constitutes the upstream-propagating component of the feedback loop at the A1 and A2 modes. However, the modified model cannot estimate the screech frequency at the B mode. Thus, the screech feedback loop at the B mode is closed by the upstream-propagating free-stream acoustic waves. Different upstream-propagating components of the feedback loops are the reason why the screech tones at the A2 and B modes can coexist.

Finally, the coherent structures associated with the screech tones are extracted by DMD. The coherent structures have the same characteristics as the corresponding screech modes. The flow structures associated with the A2 mode exhibit a slight flapping motion under the influence of the B mode.

Acknowledgements

This work was supported by the National Key R&D Program of China (grant nos. 2017YFC0111100, 2016YFC1100300), the National Natural Science Foundation of

China (grant no. 11972215), the National Numerical Windtunnel Project (grant no. NNW2019ZT2-B05) and the National Basic Research Program of China (The 973 Program) through grant no. 2012CB720100.

Declaration of interests

The authors report no conflict of interest.

Supplementary movies

Supplementary movies are available at https://doi.org/10.1017/jfm.2020.436.

REFERENCES

ANDRE, B., CASTELAIN, T. & BAILLY, C. 2011 Shock-tracking procedure for studying screech-induced oscillations. *AIAA J.*, **49** (7), 1563–1566.

BALSARA, D. S. & SHU, C.-W. 2000 Monotonicity preserving weighted essentially non-oscillatory schemes with increasingly high order of accuracy. *J. Comput. Phys.* **160** (2), 405–452.

BATCHELOR, G. K. 1953 *The Theory of Homogeneous Turbulence*. Cambridge University Press.

BERLAND, J., BOGEY, C. & BAILLY, C. 2007 Numerical study of screech generation in a planar supersonic jet. *Phys. Fluids* **19** (7), 075105.

BOGEY, C. & BAILLY, C. 2010 Influence of nozzle-exit boundary-layer conditions on the flow and acoustic fields of initially laminar jets. *J. Fluid Mech.* **663**, 507–538.

BOGEY, C. & GOJON, R. 2017 Feedback loop and upwind-propagating waves in ideally expanded supersonic impinging round jets. *J. Fluid Mech.* **823**, 562–591.

DAVIES, M. & OLDFIELD, D. 1962 Tones from a choked axisymmetric jet. I. Cell structure, eddy velocity and source locations. *Acta Acust.* **12** (4), 257–267.

EDGINGTON-MITCHELL, D. 2019 Aeroacoustic resonance and self-excitation in screeching and impinging supersonic jets – a review. *Intl J. Aeroacoust.* **18** (2–3), 118–188.

EDGINGTON-MITCHELL, D., JAUNET, V., JORDAN, P., TOWNE, A., SORIA, J. & HONNERY, D. 2018 Upstream-travelling acoustic jet modes as a closure mechanism for screech. *J. Fluid Mech.* **855**, R1.

EDGINGTON-MITCHELL, D., OBERLEITHNER, K., HONNERY, D. R. & SORIA, J. 2014 Coherent structure and sound production in the helical mode of a screeching axisymmetric jet. *J. Fluid Mech.* **748**, 822–847.

GAO, J. H. & LI, X. D. 2010 A multi-mode screech frequency prediction formula for circular supersonic jets. *J. Acoust. Soc. Am.* **127** (3), 1251–1257.

GLASS, D. R. 1968 Effects of acoustic feedback on the spread and decay of supersonic jets. *AIAA J.* **6** (10), 1890–1897.

GOJON, R. & BOGEY, C. 2017 Numerical study of the flow and the near acoustic fields of an underexpanded round free jet generating two screech tones. *Intl J. Aeroacoust.* **16** (7–8), 603–625.

GOJON, R., BOGEY, C. & MARSDEN, O. 2016 Investigation of tone generation in ideally expanded supersonic planar impinging jets using large-eddy simulation. *J. Fluid Mech.* **808**, 90–115.

GOJON, R., BOGEY, C. & MIHAESCU, M. 2018 Oscillation modes in screeching jets. *AIAA J.* **56** (7), 2918–2924.

HEISENBERG, W. 1985 Zur statistischen theorie der turbulenz. In *Original Scientific Papers Wissenschaftliche Originalarbeiten*, pp. 82–111. Springer.

HU, T. F. & MCLAUGHLIN, D. K. 1990 Flow and acoustic properties of low Reynolds-number underexpanded supersonic jets. *J. Sound Vib.* **141** (3), 485–505.

LI, X. D. & GAO, J. H. 2005 Numerical simulation of the generation mechanism of axisymmetric supersonic jet screech tones. *Phys. Fluids* **17** (8), 085105.

LI, X. D. & GAO, J. H. 2008 Numerical simulation of the three-dimensional screech phenomenon from a circular jet. *Phys. Fluids* **20** (3), 035101.

LUMLEY, J. L. 1967 The structure of inhomogeneous turbulent flows. In *Atmospheric Turbulence and Radio Wave Propagation* (ed. A. M. Yaglom & V. I. Tatarski), pp. 166–178. Nauka.

MANCINELLI, M., JAUNET, V., JORDAN, P. & TOWNE, A. 2019 Screech-tone prediction using upstream-travelling jet modes. *Exp. Fluids* **60**, 22.

MANCINELLI, M., PAGLIAROLI, T., DI MARCO, A., CAMUSSI, R. & CASTELAIN, T. 2017 Wavelet decomposition of hydrodynamic and acoustic pressures in the near field of the jet. *J. Fluid Mech.* **813**, 716–749.

MERCIER, B., CASTELAIN, T. & BAILLY, C. 2017 Experimental characterisation of the screech feedback loop in underexpanded round jets. *J. Fluid Mech.* **824**, 202–229.

MERLE, M. 1956 Sur la frequence des ondes sonores emises par un jet dair a grande vitesse. *C. R. Hebd. Seances Acad. Sci.* **243** (5), 490–493.

MORINISHI, Y., VASILYEV, O. V. & OGI, T. 2004 Fully conservative finite difference scheme in cylindrical coordinates for incompressible flow simulations. *J. Comput. Phys.* **197** (2), 686–710.

PACK, D. C. 1950 A note on Prandtl formula for the wave-length of a supersonic gas jet. *Q. J. Mech. Appl. Maths* **3** (2), 173–181.

PANDA, J. 1998 Shock oscillation in underexpanded screeching jets. *J. Fluid Mech.* **363**, 173–198.

PANDA, J. 1999 An experimental investigation of screech noise generation. *J. Fluid Mech.* **378**, 71–96.

PANDA, J. & SEASHOLTZ, R. G. 1999 Measurement of shock structure and shock–vortex interaction in underexpanded jets using Rayleigh scattering. *Phys. Fluids* **11** (12), 3761–3777.

PONTON, M. K. & SEINER, J. M. 1992 The effects of Nozzle exit lip thickness on plume resonance. *J. Sound Vib.* **154** (3), 531–549.

PONTON, M. K. & SEINER, J. M. 1995 Acoustic study of B helical mode for choked axisymmetric nozzle. *AIAA J.* **33** (3), 413–420.

POWELL, A. 1953 On the mechanism of choked jet noise. *Proc. Phys. Soc. Lond.* B **66** (408), 1039–1056.

POWELL, A., UMEDA, Y. & ISHII, R. 1992 Observations of the oscillation modes of choked circular jets. *J. Acoust. Soc. Am.* **92** (5), 2823–2836.

RAMAN, G. 1997 Screech tones from rectangular jets with spanwise oblique shock-cell structures. *J. Fluid Mech.* **330**, 141–168.

RAMAN, G. 1998 Advances in understanding supersonic jet screech: review and perspective. *Prog. Aerosp. Sci.* **34** (1–2), 45–106.

RAMAN, G. 1999 Supersonic jet screech: half-century from Powell to the present. *J. Sound Vib.* **225** (3), 543–571.

RUUTH, S. J. & SPITERI, R. J. 2004 High-order strong-stability-preserving Runge–Kutta methods with downwind-biased spatial discretizations. *SIAM J. Numer. Anal.* **42** (3), 974–996.

SCHLICHTING, H. & GERSTEN, K. 2016 *Boundary-Layer Theory*. Springer.

SCHMID, P. J. 2010 Dynamic mode decomposition of numerical and experimental data. *J. Fluid Mech.* **656**, 5–28.

SHEN, H. & TAM, C. K. W. 2002 Three-dimensional numerical simulation of the jet screech phenomenon. *AIAA J.* **40** (1), 33–41.

SIROVICH, L. 1987 Turbulence and the dynamics of coherent structures. I. Coherent structures. *Q. Appl. Maths* **45** (3), 561–571.

STEGER, J. L. & WARMING, R. F. 1981 Flux vector splitting of the inviscid gas-dynamic equations with application to finite-difference methods. *J. Comput. Phys.* **40** (2), 263–293.

SUZUKI, T. & LELE, S. K. 2003 Shock leakage through an unsteady vortex-laden mixing layer: application to jet screech. *J. Fluid Mech.* **490**, 139–167.

TAIRA, K., BRUNTON, S. L., DAWSON, S. T. M., ROWLEY, C. W., COLONIUS, T., MCKEON, B. J., SCHMIDT, O. T., GORDEYEV, S., THEOFILIS, V. & UKEILEY, L. S. 2017 Modal analysis of fluid flows: an overview. *AIAA J.* **55** (12), 4013–4041.

TAM, C. K. W. 1995 Supersonic jet noise. *Annu. Rev. Fluid Mech.* **27** (1), 17–43.

TAM, C. K. W. & AHUJA, K. K. 1990 Theoretical-model of discrete tone generation by impinging jets. *J. Fluid Mech.* **214**, 67–87.

TAM, C. K. W. & HU, F. Q. 1989 On the 3 families of instability waves of high-speed jets. *J. Fluid Mech.* **201**, 447–483.

TAM, C. K. W. & NORUM, T. D. 1992 Impingement tones of large aspect ratio supersonic rectangular jets. *AIAA J.* **30** (2), 304–311.

THOMPSON, K. W. 1987 Time-dependent boundary-conditions for hyperbolic systems. *J. Comput. Phys.* **68** (1), 1–24.

THOMPSON, K. W. 1990 Time-dependent boundary-conditions for hyperbolic systems, II. *J. Comput. Phys.* **89** (2), 439–461.

TOWNE, A., CAVALIERI, A. V. G., JORDAN, P., COLONIUS, T., SCHMIDT, O., JAUNET, V. & BRÈS, G. A. 2017 Acoustic resonance in the potential core of subsonic jets. *J. Fluid Mech.* **825**, 1113–1152.

UMEDA, Y. & ISHII, R. 2001 On the sound sources of screech tones radiated from choked circular jets. *J. Acoust. Soc. Am.* **110** (4), 1845–1858.

WALKER, S. H., GORDEYEV, S. V. & THOMAS, F. O. 1997 A wavelet transform analysis applied to unsteady aspects of supersonic jet screech resonance. *Exp. Fluids* **22** (3), 229–238.

WU, M. & MARTIN, M. P. 2007 Direct numerical simulation of supersonic turbulent boundary layer over a compression ramp. *AIAA J.* **45** (4), 879–889.